REPORT DOCUMENTATION PAGE

AFRL-SR-AR-TR-08-0026

The public reporting burden for this collection of information is estimated to average 1 hour per response, including the ti gathering and maintaining the data needed, and completing and reviewing the collection of information. Send comments regar information, including suggestions for reducing the burden, to the Department of Defense, Executive Services and Commun that notwithstanding any other provision of law, no person shall be subject to any penalty for failing to comply with a colle control number.
PLEASE DO NOT RETURN YOUR FORM TO THE ABOVE ORGANIZATION.

1. REPORT DATE *(DD-MM-YYYY)*	2. REPORT TYPE	3. DATES COVERED *(From - To)*
	FINAL REPORT	01 Dec 2003 - 31 May 2007

4. TITLE AND SUBTITLE
FEMTOSCEOND OPTICS: ADVANCED DEVICES AND ULTRAFAST PHENOMENA

5a. CONTRACT NUMBER

5b. GRANT NUMBER
FA9550-04-1-0011

5c. PROGRAM ELEMENT NUMBER
61102F

6. AUTHOR(S)
PROFESSOR IPPEN

5d. PROJECT NUMBER
2301/AX

5e. TASK NUMBER

5f. WORK UNIT NUMBER

7. PERFORMING ORGANIZATION NAME(S) AND ADDRESS(ES)
MASSACHUSETTS INSTITUTE OF TECHNOLOGY
77 MASSACHUSETTS AVENUE
CAMBRIDGE MA 02139

8. PERFORMING ORGANIZATION REPORT NUMBER

9. SPONSORING/MONITORING AGENCY NAME(S) AND ADDRESS(ES)
AF OFFICE OF SCIENTIFIC RESEARCH
875 NORTH RANDOLPH STREET ROOM 3112
ARLINGTON VA 22203
DR HOWARD SCHLOSSBERG/NE

10. SPONSOR/MONITOR'S ACRONYM(S)

11. SPONSOR/MONITOR'S REPORT NUMBER(S)

12. DISTRIBUTION/AVAILABILITY STATEMENT
DISTRIBUTION STATEMEN A: UNLIMITED

13. SUPPLEMENTARY NOTES

14. ABSTRACT
ON SEPARATE SHEET

15. SUBJECT TERMS

16. SECURITY CLASSIFICATION OF:			17. LIMITATION OF ABSTRACT	18. NUMBER OF PAGES	19a. NAME OF RESPONSIBLE PERSON
a. REPORT	b. ABSTRACT	c. THIS PAGE			19b. TELEPHONE NUMBER *(Include area code)*

Status and Accomplishments

Over the three years of this program we have made significant achievements in several areas: development of new femtosecond laser systems and ultrafast optical techniques, application of ultrafast optics to waveguide and fiber devices, designs and studies of novel materials and material structures. These are documented by 36 publications in refereed journals and 3 patent applications, a list of which is given at the end of this report as indicated below. Some of the key achievements are described in sections entitled:

A. Phase-Coherent Spectrum from the Visible to the Infrared by Combining Ultrabroadband Ti:sapphire and Cr:forsterite Lasers
B. Resonant Silicon-Germanium Saturable Bragg Reflectors
C. Cavity Enhanced Optical Parametric Chirped Pulse Amplification
D. Passively Modelocked High-Rep-Rate Erbium-doped Bismuth Oxide Glass Waveguide Laser
E. Frequency Combs at High Repetition Rates Using Fiber Lasers and Supercontinuum Generation
F. Ultrafast Optical Switching and Wavelength Conversion
G. Continuum Generation in Photonic Crystal Fibers for Optical Coherence Tomography
H. Frequency Swept Lasers and Fourier Domain Mode Locking (FDML)
I. Physics of X-Ray Generation: The Ehrenfest Theorem and the Single Atom HHG Spectrum
J. The Role of Many Electron Effects in High Harmonic Generation
K. Broadband Studies of 1-D and 3-D Photonic Crystals
L. Ultrawide Tuning of Photonic Microcavities via Evanescent Field Perturbation
M. Propagation without Diffraction in a 2D Photonic Crystal
N. Laser Micromachining of Photonic Devices

Publications in refereed journals acknowledging FA9550-04-001 1

FINAL REPORT 2004-2006

Air Force Office of Scientific Research
Contract: FA9550-04-0011

FEMTOSECOND OPTICS: ADVANCED DEVICES AND ULTRAFAST PHENOMENA

Principal Investigators

Professor Erich P. Ippen
Professor James G. Fujimoto
Professor Franz Kaertner

Address

The Research Laboratory of Electronics
Massachusetts Institute of Technology
77 Massachusetts Avenue
Cambridge, MA 02139

20080124171

FINAL REPORT

Period: December 1, 2003 – November 30, 2006

Air Force Office of Scientific Research

Contract: FA9550-04-0011

Principal Investigators

Professor Erich P. Ippen
Professor James G. Fujimoto
Professor Franz Kaertner

Contributing Staff

Dr. Yu Chen, Dr. Richard Ell, Dr. Ariel Gordon, Dr. Robert Huber, Dr. Omer Ilday, Dr. Oliver Muecke, Dr. Alphan Sennaroglu, Dr. Hideyuki Sotobayashi, Dr. Philipp Wagenblast, Aaron Aguirre, Jonathan Birge, Hyunil Byun, Jeff Chen, Marcus Dahlem, Fuwan Gan, Juliet Gopinath, Felix Grawert, Matthew Grein, Paul Herz, Leaf Jiang, Christian Jirauschek, Jungwon Kim, Andrew Kowalevicz, Tieming Liu, Poh Poon Phua, Milos Popovic, Rohit Prasankumar, Peter Rakich, Vikas Sharma, Hanfei Shen, Jason Sickler and Michael Watts.

Objectives

To investigate fundamental femtosecond-timescale phenomena in materials and devices. To evaluate the potential of these phenomena and structure for applications. To invent and demonstrate new devices for ultrafast optics.

Status and Accomplishments

Over the three years of this program we have made significant achievements in several areas: development of new femtosecond laser systems and ultrafast optical techniques, application of ultrafast optics to waveguide and fiber devices, designs and studies of novel materials and material structures. These are documented by 36 publications in refereed journals and 3 patent applications, a list of which is given at the end of this report as indicated below. Some of the key achievements are described in sections entitled:

A. Phase-Coherent Spectrum from the Visible to the Infrared by Combining Ultrabroadband Ti:sapphire and Cr:forsterite Lasers
B. Resonant Silicon-Germanium Saturable Bragg Reflectors
C. Cavity Enhanced Optical Parametric Chirped Pulse Amplification
D. Passively Modelocked High-Rep-Rate Erbium-doped Bismuth Oxide Glass Waveguide Laser
E. Frequency Combs at High Repetition Rates Using Fiber Lasers and Supercontinuum Generation
F. Ultrafast Optical Switching and Wavelength Conversion
G. Continuum Generation in Photonic Crystal Fibers for Optical Coherence Tomography
H. Frequency Swept Lasers and Fourier Domain Mode Locking (FDML)
I. Physics of X-Ray Generation: The Ehrenfest Theorem and the Single Atom HHG Spectrum
J. The Role of Many Electron Effects in High Harmonic Generation
K. Broadband Studies of 1-D and 3-D Photonic Crystals
L. Ultrawide Tuning of Photonic Microcavities via Evanescent Field Perturbation
M. Propagation without Diffraction in a 2D Photonic Crystal
N. Laser Micromachining of Photonic Devices

Publications in refereed journals acknowledging FA9550-04-0011

A: Phase-Coherent Spectrum from the Visible to the Infrared by Combining Ultrabroadband Ti:sapphire and Cr:forsterite Lasers

Coherent superposition of multiple mode-locked lasers has been recognized as one of the most promising techniques to generate well-isolated, highly-stable single-cycle optical pulses beyond the bandwidth limitations of gain media and laser mirrors. To synthesize single-cycle optical pulses, we have worked on the synthesis of optical combs spanning from the visible to the infrared range from mode-locked Ti:sapphire and Cr:forsterite lasers. As one step closer toward the single-cycle pulse synthesis, we present the generation of a phase-coherent spectrum [1] spanning from 600 nm to 1500 nm from a long-term stable Ti:sapphire and Cr:forsterite laser system with residual timing and phase rms-jitters of 375 as and 570 as, respectively.

Figure A1 shows the schematic of the synchronization set-up. Ultrabroadband Ti:sapphire (600-1200nm) and Cr:forsterite (1100-1500nm) lasers are combined at the broadband 50:50 beam splitter [2]. For timing synchronization, a balanced cross-correlator [3] is used. Once tight synchronization between the two laser pulses is obtained, a heterodyne beat signal between the two lasers in the spectral overlap region is obtained. This beat signal is locked to a local oscillator (f_{LO} in Fig. A1) by modulating the pump power of the Ti:sapphire laser with an AOM.

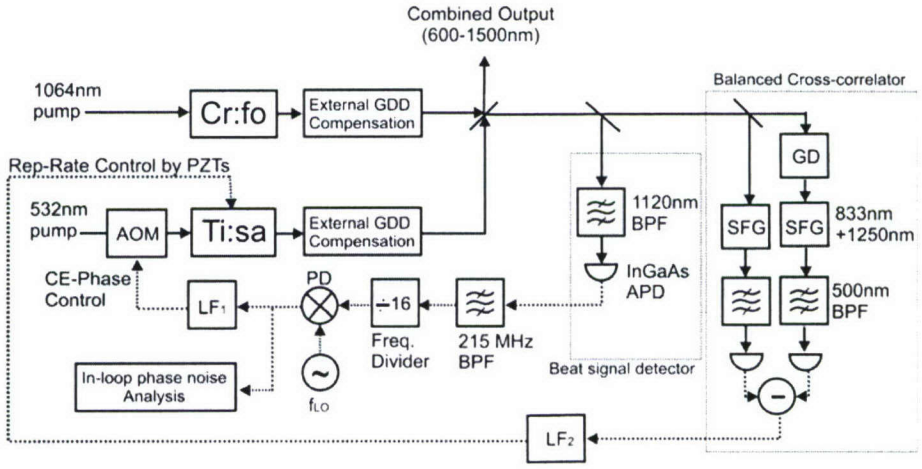

Figure A1: Schematic outline of the synchronization set-up. AOM, acousto-optic modulator; APD, Avalanche photodiode; BPF, band-pass filter; Cr:fo, Cr:forsterite laser oscillator; GD, group delay element; GDD, group delay dispersion; LF, loop filter; PD, digital phase detector; SFG, sum frequency generation; Ti:sa, Ti:sapphire laser oscillator.

To lock the difference in carrier-envelope offset frequency, Δf_{ceo}, between the two lasers, we filter out a 15 nm wide part of the spectrum in the overlap spectral range at 1120 nm and detect it with a high-speed InGaAs Avalanche photodetector. Fig. A2 (a) shows the RF spectrum of the output from the photodetector. Heterodyne beatnotes ($mf_R \pm \Delta f_{ceo}$, m=integer) show ~30 dB SNR measured with a 30 kHz resolution bandwidth. The beatnote at 215 MHz is bandpass filtered, amplified, and frequency divided by a factor of 16 to increase the locking range. This beatnote is locked to an RF synthesizer, f_{LO}, at ~13.43 MHz via modulating intra-cavity energy of the Ti:sapphire laser with an AOM (see Fig. A1).

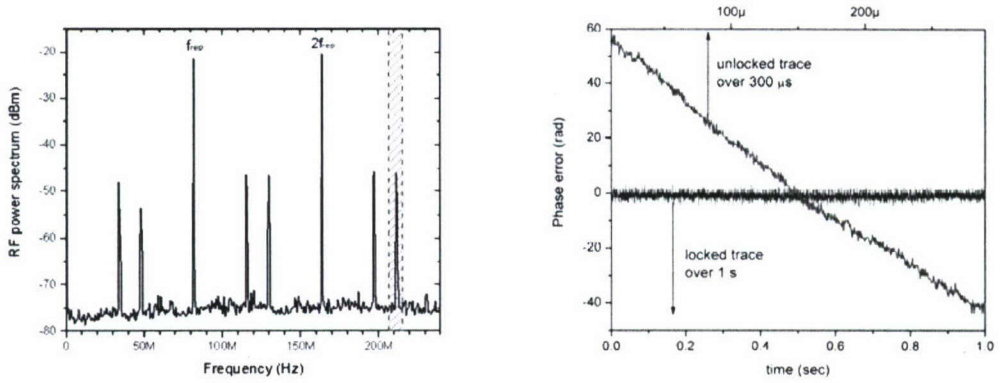

(a) (b)

Figure A2: (a) RF spectrum (RBW 30 kHz) of the beat signals from the InGaAs APD output in Fig. A1. Red shadowed region indicates the bandpass filter centered at 215 MHz that selects the beat signal used for phase-locking. (b) In-loop phase error signal from the digital phase detector (PD in Fig. A1). Red line shows the free-running phase error signal over 300 μsec time scale. Blue line shows the residual in-loop phase error for 1 second when it is locked. The residual phase jitter from 1 Hz to 1 MHz is 0.38π rad (570 as). Note that the phase errors shown here are already scaled to the full range, i.e., [-16π, +16π] range.

Figure A2(b) shows the output from the digital phase detector for the free-running and locked states with two different time scales (300 μs and 1 s respectively). When it is locked, the in-loop integrated rms phase noise is 0.38π radians measured from 1 Hz to 1 MHz. This is equivalent to 570 as rms phase jitter from 1 Hz to 1 MHz. To our knowledge this is the lowest reported phase jitter between two independent mode-locked lasers [4]. The main reason for this improvement is due to the very low timing jitter between the two lasers achieved by the balanced cross-correlator. Further improvements are clearly possible by optimization of the phase-locked loop and noise reduction in the Cr:forsterite laser which seems to be the main reason for the large remaining carrier-envelope phase noise. This large noise currently prevents us from locking the difference carrier-envelope frequency to zero by homodyne detection and synthesizing a single-cycle pulse. Note, this cannot be achieved with conventional offset locking in a long-term stable way because offset locking introduces an uncontrolled path difference between the two laser outputs.

In conclusion, we have presented a phase-coherent ultrabroadband optical spectrum ranging from the visible to the infrared by timing synchronization and phase-locking of mode-locked Ti:sapphire and Cr:forsterite lasers. In addition to the low sub-femtosecond timing jitter demonstrated previously [3], a sub-femtoseond rms phase jitter between the two lasers of 0.38π rad (570 as) measured from 1Hz to 1MHz is demonstrated. It is expected that further noise reduction enables a phase jitter much less than 2π which opens up the possibility to generate single-cycle pulses at 1 μm from a long-term stable setup.

References:

[1] J. Kim, T. R. Schibli, L. Matos, H. Byun and F. X. Kaertner, "Phase-coherent spectrum from ultrabroadband Ti:sapphire and Cr:forsterite lasers covering the visible to the infrared", Proceedings of Ultrafast Optics Conference 2005, Paper M3-5, Nara, Japan, Sept 2005.

[2] J. Kim, J. R. Birge, V. Sharma, J. G. Fujimoto, F. X. Kaertner, V. Scheuer, G. Angelow, "Ultrabroadband beam splitter with matched group delay dispersion", Opt. Lett. 30, 1569 (2005).

[3] T.R. Schibli, J. Kim, O. Kuzucu, J. Gopinath, S.N. Tandon, G.S. Petrich, L.A. Kolodziejski, J.G. Fujimoto, E.P. Ippen, and F.X. Kaertner, Opt. Lett. 28, 947 (2003).

[4] A. Bartels, N. R. Newbury, I. Thomann, L. Hollberg, and S. A. Diddams, Opt. Lett. 29, 403 (2004).

B: Resonant Silicon-Germanium Saturable Bragg Reflectors

We demonstrate that resonant coatings on a Saturable Bragg Reflector (SBR) can lower the saturation fluence and increase the modulation depth by enhancing the field intensity inside the absorber layer. In this report, we show that our resonant silicon-germanium SBRs reduced the saturation fluence by factor of four and also increased the modulation depth that much.

An SBR can be used to passively mode-lock a laser by its intrinsic property of an intensity-dependent reflectivity. An SBR is composed of an absorber layer on the dielectric mirror stack. For the absorber layer, III-V compound semiconductor materials began to be used first, but nowadays research on column-IV semiconductor such as silicon or germanium is actively going on for the purpose of pursuing compatibility with CMOS process.

At higher repetition rates inr a mode-locked laser, the fluence on the saturable absorber decreases for two reasons. First, the length of cavity should become smaller since the repetition rate of pulse trains is inversely proportional to the cavity length. Consequently if mirrors stay with same curvature, the spot size on the absorber gets larger. This causes smaller fluence for a given pulse energy. Second, the higher repetition rate reduces the pulse energy when we assume that the intracavity power remains same. The fluence decreases for a given spot size on the absorber. If the fluence is not high enough on the absorber surface, a mode-locked laser is more likely to fall into the Q-switched mode-locked regime instead of continuous wave mode-locked operation.

In order to overcome this problem, the necessary fluence for a saturable absorber to be CW mode-locked was lowered by putting additional coatings which enhances the field intensity around the absorber layer. These coatings are called the resonant coating. A resonantly-coated SBR has lower saturation fluence and bigger modulation depth than those of an SBR without resonant coating since the field intensity at the absorber layer is increased.

Two kinds of resonant coatings were designed, three-layer structure and five-layer one. As more layers are deposited for resonance, the reflectivity of the coatings increase and the field in the absorber layer is more enhanced as shown in the previous subsection. Target field intensity for those resonant coatings is shown in Table B1. The figures in Table B1 are simulation results from the OptiLayer software. We can see that the peak field in the germanium layer almost doubles when one pair of resonant coatings is added.

Table B1. Layer thickness for resonant coatings.

	3-layers	5-layers
Original SBR	-	-
SiO_2	534nm	560nm
Ta_2O_5	181nm	190nm
SiO_2	267nm	280nm
Ta_2O_5	0nm	190nm
SiO_2	0nm	280nm
Air	-	-

Table B2. Absorption and peak field intensity depending on the number of layers of resonant coatings. The intensity of incident beam is set to 100% for a relative comparison.

	Absorption at 1550nm	Peak field intensity in Ge layer
No resonant coating	0.75%	32%
3-layers	1.6%	67%
5-layers	3.0%	130%

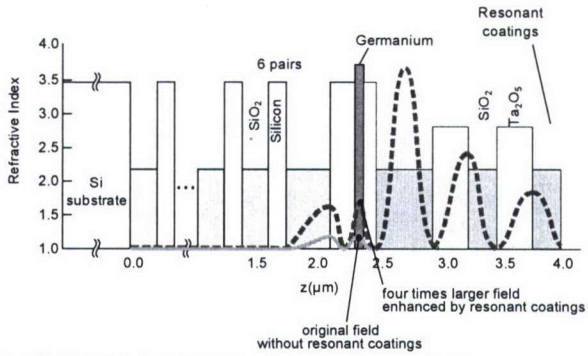

Figure B1. Structure of SiGe-SBR with five layers of resonant coatings

In order to achieve the field enhancement in Table B1, resonant coatings were deposited on the original SBR structure by Peter O'Brien at MIT Lincoln Laboratory (Figure B1). The thickness of each coating is specified in Table B2. The low-index material closer to the original structure starts with half wavelength thickness and the subsequent layers are quarter wavelength thick to function as a reflector.

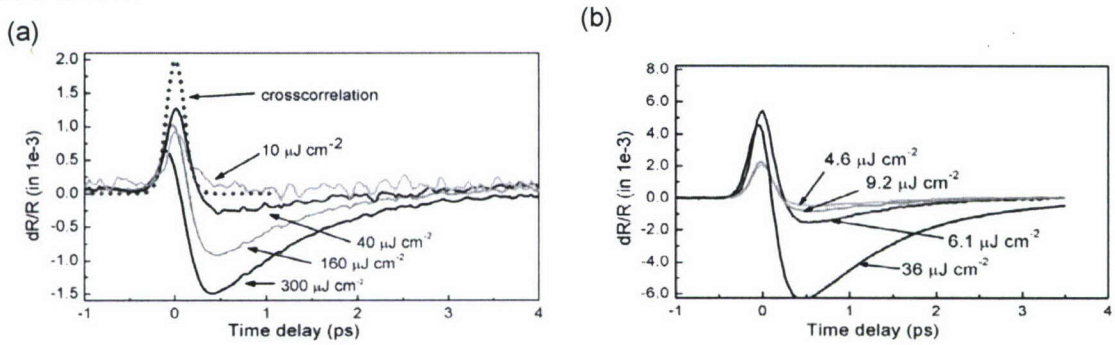

Figure B2: (a) Pump-probe traces of the previous SiGe-SBR without resonant coatings. (b) Pump-probe traces of the resonantly-coated SiGe-SBR taken at various fluence values.

The nonlinear response of the device was characterized using a pump-probe measurement setup with 150fs pulse centered at 1540nm (Figure B2). A fluence of 9.2 uJ/cm^2 was needed to give maximum modulation depth of 0.52%. This modulation depth is four times larger than that of the previous SBR and the corresponding fluence is four times smaller. These measurement results agree with the simulation where the field intensity was enhanced by factor of four.

Although resonant coatings can provide enhanced absorption and modulation depth, they can bring unwanted side effects. With those resonant coatings, the field intensity increases not only in the absorber layer but also in the neighboring layers. The increased intensity in the neighboring layers can cause larger nonsaturable loss which can destabilize CW mode locking. Therefore it is important to use material with as low loss as possible.

In conclusion, we developed resonant silicon germanium SBRs which have smaller saturation fluence and higher modulation depth by factor of four compared to SBRs without resonant coatings. These SBRs can be applied to passively mode-locked lasers with higher repetition rate where the pulse energy gets smaller below mode-locking threshold.

References

1) Felix J. Grawert. PhD Thesis, MIT, 2005
2) F. J. Grawert, S. Akiyama, J. T. Gopinath, F. O. Ilday, J. Liu, H. Shen, K. Wada, L. C. Kimerling, E. P. Ippen and F. X. Kärtner, Appl. Phys. Lett. 74, 3927~3929 (1999)

C: Cavity-Enhanced Optical Parametric Chirped-Pulse Amplification

Development of robust and inexpensive techniques for the amplification of few-cycle pulses will have tremendous impact in diverse fields, including high-harmonic generation. Recently, coherent addition of pulses in an enhancement cavity has been proposed and demonstrated as a method of short-pulse amplification [1]. However, this method gets increasingly difficult for short pulses due to intra-cavity dispersion and self-phase modulation. Lately, there is much interest in optical parametric chirped-pulse amplification (OPCPA) [2]. Utilizing virtual energy states, there is no storage of the pump light in parametric amplification, necessitating synchronous pumping with comparable pump and signal pulse durations. Thus, a high-energy pump source with picosecond pulses and excellent beam quality is required.

Here, we report a novel scheme, which conceptually combines the OPCPA and enhancement cavity techniques (Fig. C1): The pump beam is coherently enhanced in an external cavity, which contains a nonlinear crystal phase-matched for parametric amplification of a signal pulse. The cavity is transparent at the signal wavelength. The stretched signal pulses are synchronized and time-gated to overlap spatially and temporally with the pump beam and undergo parametric amplification once the cavity is loaded. This way, signal pulses with a bandwidth supporting few-cycle pulses can be amplified without the limitations set by the cavity. Cavity-enhanced OPCPA extends the analogy of parametric amplification to regular amplification one step further; the cavity assumes the role of pump light storage with the product of the cavity roundtrip time and the finesse corresponding to the gain relaxation time.

Several major advantages can be identified. The pump light itself can be in the picosecond range or longer, thus dispersion ceases to be a limitation to the enhancement cavity. With increasing finesse of the cavity, the pump source has only to provide lower peak powers, opening up the use of laser sources which excel in high average power, but are limited in peak power, such as fiber amplifiers. The high-finesse cavity will act as an excellent spatial filter for the pump beam, ensuring a high beam quality for the amplified pulse.

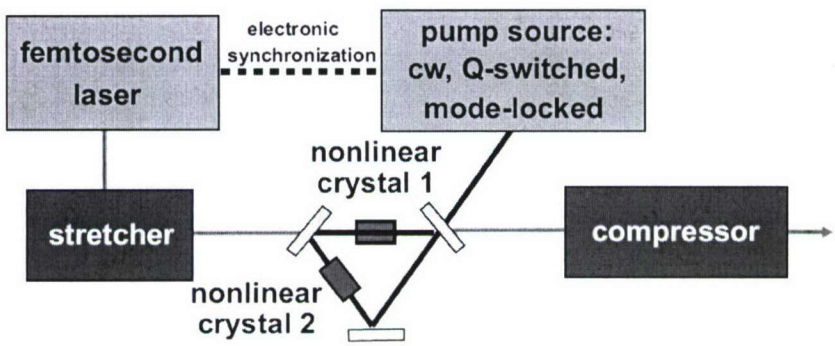

Fig. C1. Schematic of the cavity-enhanced OPCPA. Nonlinear crystal 1 and (optional) nonlinear crystal 2 are for parametric amplification and nonlinearity management, respectively.

The dynamics of the cavity-enhanced OPCPA can be understood in two independent steps, which can be analyzed separately. During the loading phase, the nonlinear crystal is a passive element. Once the cavity is fully loaded, the signal pulse is triggered and makes a single pass through the cavity. Thus, parametric amplification is not influenced by the enhancement cavity. Then, the entire sequence is repeated.

Pump enhancement factors approaching 50 and parametric gain larger than 20 dB can be realized with 1.0μm pump and 1.55 μm signal, using periodically poled lithium niobate (PPLN), which already represents a significant advance. Gain is given by $G=0.25(1+ \exp(gl))$, where for

PPLN, $g = 5.2\ I_p/(GW/cm^2)^{0.5}/mm$. Thus, for an intensity of about 0.5 GW/cm^2 in a 2 mm-long crystal, input to output gain of about 26dB is achieved. The peak phase shift due to the Kerr nonlinearity per roundtrip in the crystal is 5.6×10^{-3}, which allows for an addition of about 50 pulses.

At higher peak powers, Kerr nonlinearity will eventually pose a limitation by causing the cavity modes to shift dynamically. We show that this can be overcome by nonlinearity management utilizing cascaded quadratic processes [3]. These processes provide self-defocusing Kerr nonlinearity, permitting temporal and spatial compensation of n_2 to first order [4]. We numerically simulated the loading of a cavity with a pulse train from a high-power laser at 1064 nm. The cavity comprises a 2 mm-long BBO crystal for parametric amplification and dispersion-compensating mirrors. A spot size of r=60 μm in a 2 mm-long crystal results in a nonlinear phase shift per roundtrip of 3.6×10^{-2}rad/MW. For nonlinearity compensation with the cascade process, another BBO crystal of equal length is added. The benefits of nonlinearity management are illustrated in Fig. 2(a). The cavity finesse is 100π. Without compensation, about 50 pump pulses can be added up to reach an intra-cavity pulse power of 0.5 MW. Due to the less favorable $\chi^{(2)} / \chi^{(3)}$ ratio of BBO, this leads to a maximum parametric gain of only 7.6 dB. Using nonlinearity compensation, pump pulses with even 100 times higher peak power can attain the theoretical limit of 100 times enhancement. At a peak power of 5 MW, small-signal parametric gain of 37 dB is expected. In these calculations, the pulse duration is fixed at 10 ps. For shorter pulses, the buildup process becomes complicated due to the interplay of nonlinearity and dispersion (Fig. 2(b)). Nonlinearity management becomes even more crucial in experiments utilizing nonlinear crystals with less favorable ratios of gain to self-phase modulation.

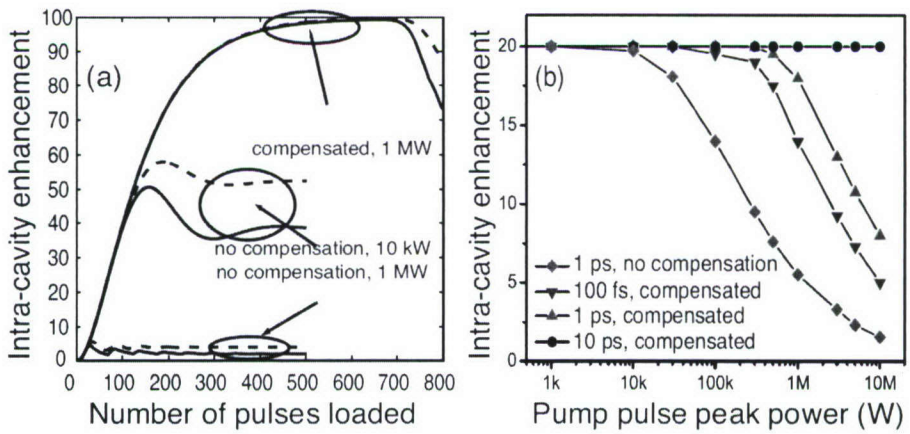

Fig. C2. Results of numerical simulations: (a) Loading of the cavity with and without nonlinearity compensation. Solid (dashed) lines depict intra-cavity energy (peak power) enhancement. (b) Intra-cavity buildup factor as a function of the peak power of the pump pulses with and without compensation of the nonlinearity. The lines connecting the dots are only a guide to the eye.

In conclusion, we propose a new technique, cavity-enhanced OPCPA as a practical route to high average and peak power sources of few-cycle optical pulses. The role of the cavity is analogous to the storage of pump light in an excited atomic state in regular amplification. In order to reach even higher energies, nonlinearity management can be utilized. Practical implementation of this scheme using fiber lasers is underway. Thus far, we have obtained single-pass OPCPA using an Er-fiber laser, synchronized with a Yb-fiber laser, which seeds a solid-state amplifier. The enhancement cavity is currently under construction.

References

[1] E. O. Potma, C. Evans, X. S. Xie, R. J. Jones, and J. Ye, "Picosecond-pulse amplification with an external passive optical cavity," Opt. Lett. 28, 1835 (2003).

[2] A. Dubietis, G. Jonusauskas, A. Piskarskas, "Powerful fs pulse generation by chirped and stretched pulse parametric amplification in BBO crystal," Opt. Commun. 88, 433 (1992).
[3] F. Ö. Ilday, and F. W. Wise, "Nonlinearity management: a route to high-energy soliton fiber lasers," J. Opt. Soc. Am. B 19, 470-476 (2002).
[4] F. Wise, L. Qian, X. Liu, "Applications of cascaded quadratic nonlinearities to femtosecond pulse generation," J. Nonlin. Opt. Phys. Mat. 11, 317-338 (2002), and references therein.

D: Passively Modelocked High-Repetition Rate Erbium-doped Bismuth Oxide Glass Waveguide Laser

The development of novel broadband light sources at 1.5 μm is strongly motivated by the widespread application of WDM technology and is key to expanding the usable bandwidth of optical transmission systems. In addition, in combination with external supercontinuum generation, these sources have the potential to be compact, stable, high-bandwidth optical oscillators, with applications in optical metrology, ultra-wideband optical communications, sub-diffraction-limit imaging, and optical arbitrary waveform generation.

Rare-earth doped glass amplifiers are particularly promising. Thulium-doped glass amplifiers can provide gain in the 1480-1510 nm wavelength range. Erbium-doped tellurite glass have a gain bandwidth of 70 nm centered around 1530 nm that covers the conventional gain bandwidth of silica-based erbium-doped glasses as well as somewhat longer wavelengths. The widest emission band from erbium-doped glasses in the 1.5 μm wavelength range have been reported in a Bi_2O_3-B_2O_3-SiO_2 system [1], making it an attractive alternative and a strong candidate for use in a modelocked laser. In addition to the broad bandwidth, the erbium doping can be much higher in a bismuth-oxide glass host than in conventional silica, offering the possibility of a significant reduction in the device length needed for laser gain. This makes the material attractive for short-cavity high-repetition-rate systems.

Both cw signal amplification [2] and picosecond pulse amplification [3] over the wavelength range of 1520-1600 nm using a bismuth oxide-based erbium-doped fiber amplifier have been observed. In addition, wavelength-tunable passive modelocking from 1570 nm to 1600 nm was demonstrated with a bismuth oxide-based erbium-doped fiber laser [4]. We look to extend this work with a bismuth oxide-based erbium-doped waveguide laser, whose short cavity length would enable us to achieve GHz repetition rates.

Our collaborators at Asahi Glass Company (Japan) have provided us with sample waveguides in 2 cm and 6 cm lengths. Several waveguides of height 3.5 μm and widths ranging from 3-7 μm are written on each sample chip. Figure D1(a) below is a picture of one of these waveguides being diode pumped at 977 nm through a tapered lensed fiber. Figure D1(b) shows the spectral gain profile of a sample waveguide.

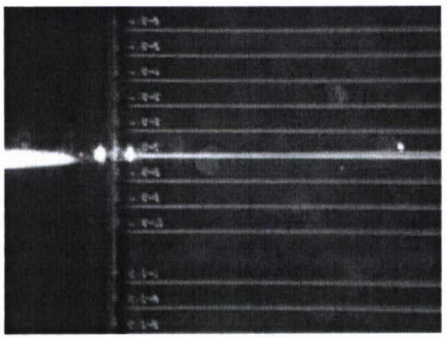

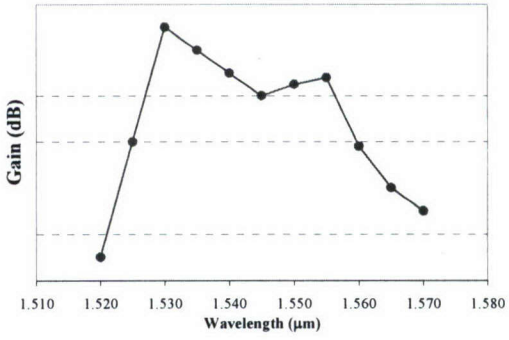

Figure D1. (a) Bismuth oxide-based erbium-doped waveguide being pumped at 977 nm through a tapered lensed fiber. (b) Spectral gain profile of a sample waveguide.

We are currently working towards demonstrating cw lasing in the waveguide laser. Once completed, we plan to modelock the waveguide laser using an ultra-broadband silicon/germanium saturable Bragg reflector (SBR) designed for high repetition rates [5]. The proposed cavity layout is shown in Figure D2. With this setup, we hope to achieve shorter pulses and higher repetition rates than previously demonstrated erbium-doped waveguide systems. In addition, together with extra-cavity amplification and smooth broadband supercontinuum generation with highly nonlinear bismuth-oxide fiber [6], we hope to demonstrate a stable frequency comb spanning the 1-2 μm wavelength range.

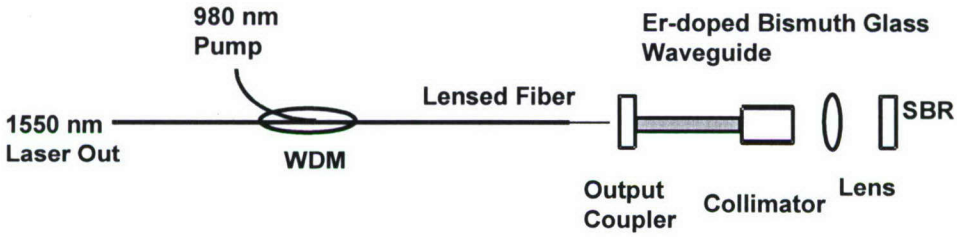

Figure D2. Cavity layout for the erbium-doped bismuth-oxide waveguide laser.

References:

1. S. Tanabe, N. Sugimoto, S. Ito, and T. Hanada, "Broad-band 1.5 m emission of Er^{3+} ions in bismuth-based oxide glasses for potential WDM amplifier," Journal of Luminescence 87-89, 670 (2000).
2. N. Sugimoto, "Ultrafast optical switches and wavelength division multiplexing amplifiers based on bismuth oxide glasses," Journal of the American Ceramic Society 85, 1083 (2002).
3. H. Sotobayashi, J.T. Gopinath, and E.P. Ippen, "23 cm long Bi_2O_3-based EDFA for picosecond pulse amplification with 80 nm gain bandwidth," IEEE Electronics Letters 39, 1374 (2003).
4. H. Sotobayashi, J.T. Gopinath, E.M. Koontz, L.A. Kolodziejski, and E.P. Ippen, "Wavelength tunable passively modelocked bismuth oxide-based erbium-doped fiber laser," Optics Communications 237, 399 (2004).
5. F.J. Grawert, J.T. Gopinath, F.O. Ilday, H.M. Shen, E.P. Ippen, F.X. Kärtner, S. Akiyama, J. Liu, K. Wada, and L.C. Kimmerling, "220-fs erbium-ytterbium:glass laser mode locked by a broadband low-loss silicon/germanium saturable absorber," Optics Letters 30, 329 (2005).
6. J.T. Gopinath, H.M. Shen, H. Sotobayashi, E.P. Ippen, T. Hasegawa, T. Nagashima, and N. Sugimoto, "Highly nonlinear bismuth oxide fiber for supercontinuum generation and femtoseconds pulse compression," Journal of Lightwave Technology 23, 3591 (2006).

E: Frequency Combs at High Repetition Rates Using Fiber Lasers and Supercontinuum Generation

The development of stable optical frequency combs based on mode-locked lasers has advance rapidly over the past decade [1-4]. These stable combs are proving useful in a number of applications, most notably in frequency metrology [2] where the comb is locked to a stable frequency reference (such as an atomic transition) and thus serves as a frequency "ruler".

Another application of stable frequency combs is in optical arbitrary waveform generation. In this application, each frequency component's amplitude and phase is independently controlled, and the resulting frequency components are superposed. In this way the Fourier construction of an arbitrary optical waveform is accomplished.

In order to generate a stable frequency comb, two parameters must be controlled. First, the spacing of the comb frequencies must be stabilized. This corresponds to stabilizing the repetition rate of the laser and can be achieved by a number of locking techniques [5]. Second, the carrier-envelope offset (CEO) frequency must be locked. In the frequency domain, this corresponds to a shift of the frequency comb from zero frequency. In the time domain, this corresponds to a changing delay between the carrier and the pulse envelope and results from a difference in the group and phase velocities. One technique for locking the carrier-envelope phase involves generating an octave-spanning comb from the laser source, and then frequency doubling the low-frequency portion of the comb to overlap with the high-frequency portion. The difference frequency is detected to measure the CEO frequency.

Our work seeks to develop a stabilized frequency comb source in the 1550 nm wavelength range using mode-locked fiber lasers in the context of developing an optical arbitrary waveform generator. Because the spectra from such lasers are generally not octave-spanning, the output of these lasers will be coupled into nonlinear fibers to generate octave-spanning supercontinuum spectra, which may then be used to stabilize the mode-locked fiber laser frequency comb [3, 4]. Initial efforts seek to accomplish this at 1 GHz repetition rates, with plans to later develop 10 GHz and 40 GHz systems.

Previous work on regeneratively-synchronized, harmonically mode-locked, fiber lasers demonstrated 1 GHz repetition rate from a soliton fiber laser [6]. Because the mode-locking mechanism is passive, no external oscillator is required, leading to a more simple locking system and, in most cases, lower noise. Figure E1 shows the layout of this system, including the regenerative synchronization loop used for harmonic mode-locking. The intra-cavity etalon will suppress amplitude and timing noise, particularly noise corresponding to the occurrence of pulse dropouts/pairs. The laser repetition rate will be locked to the etalon; the required locking electronics for this are still in development, and are not shown.

The required octave-spanning supercontinuum spectrum will be generated with highly nonlinear fibers (HNLFs). The 1 GHz laser output will first be amplified, and then coupled into an HNLF to generate the supercontinuum spectra. Figure E2 illustrates the envisioned final state of the system, with estimates of the powers and pulse durations occurring at various points. Efforts to prepare the optical pulse train and to find the appropriate HNLF are currently in progress.

The current state of the supercontinuum generation system is simpler than that shown in Figure E2. It consists of a pre-amplifier, a pulse shortening fiber, and HNLF, in that order. Figure E3 shows results from this system. With improved pulse powers, broader octave-spanning supercontinuum spectra should be achievable.

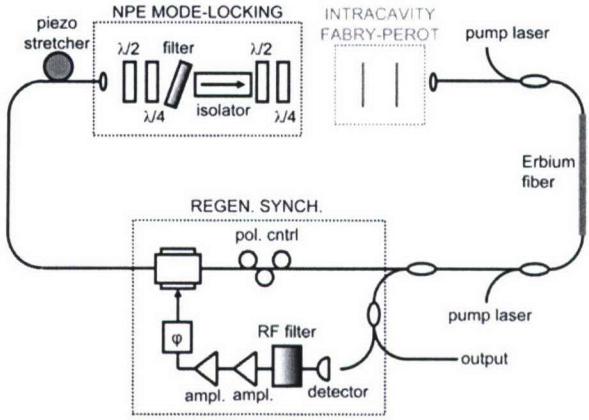

Figure E1. The harmonically mode-locked, regeneratively synchronized fiber laser. The intracavity etalon will filter amplitude and phase noise, and serve as the reference cavity for repetition rate stabilization. Stabilization electronics that lock the laser to the etalon are not shown.

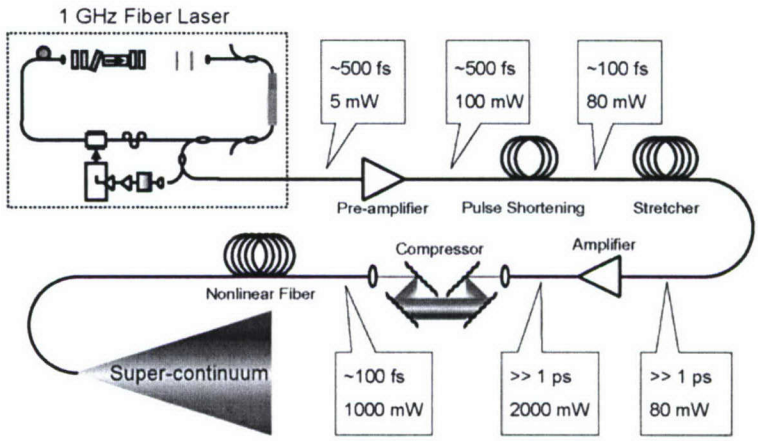

Figure E2. The supercontinuum generating system.

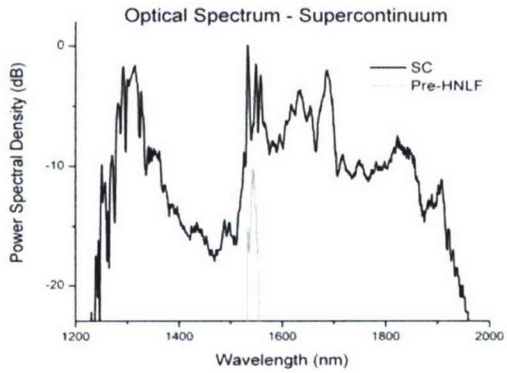

Figure E3. The power spectra densities for the amplified laser output before the HNLF (gray), and the resulting supercontinuum spectrum (black).

References:

1. Jones, D.J., et al., Carrier-envelope phase control of femtosecond mode-locked lasers and direct optical frequency synthesis. Science, 2000. 288(5466): p. 635-639.
2. Diddams, S.A., et al., Direct Link between Microwave and Optical Frequencies with a 300 THz Femtosecond Laser Comb. Phys. Rev. Lett., 2000. 84(22): p. 5102-5105.

3. Tauser, F., A. Leitenstorfer, and W. Zinth, Amplified femtosecond pulses from an Er:fiber system: Nonlinear pulse shortening and self-referencing detection of the carrier-envelope phase evolution. Opt Express, 2003. 11(6).
4. Hong, F.-L., et al., Broad-spectrum frequency comb generation and carrier-envelope offset frequency measurement by second-harmonic generation of a mode-locked fiber laser. Opt. Lett., 2003. 28(17): p. 1516-1518.
5. Drever, R.W.P., et al., Laser phase and frequency stabilization using an optical resonator. Appl. Phys. B (Photophysics and Laser Chemistry), 1983. B31(2): p. 97-105.
6. Yu, C.X., et al., Gigahertz-repetition-rate mode-locked fiber laser for continuum generation. Opt. Lett., 2000. 25(19): p. 1418-1420.

F: Ultrafast Optical Switching and Wavelength Conversion

To accommodate the increasing demand for higher bit rate optical communication, a new generation of optical communication networks is being developed in which optical-to-electrical conversion bottlenecks will be minimized by keeping the data in the optical domain. Such all-optical networks require advanced photonic technologies for a variety of ultrafast all-optical signal processing functions including optical logic and wavelength conversion. An important focus of our research is to study the ultrafast dynamics of active and nonlinear semiconductor devices for potential application to such processing.

A device that can be used as both a wavelength converter and an ultrafast optical logic gate is the integrated SOA-based Mach-Zehnder (MZ) interferometer [1,2]. This device takes advantage of nonlinear cross-phase modulation between optical signals in the semiconductor amplifier (SOA) segments. The differential phase between the two SOA arms of the interferometer can be optically controlled via input optical (control) signals entering the two arms. A schematic of such a device, being designed and fabricated in Prof. Leslie Kolodziejski's group, is shown in Figure F1. The designs of individual component structures in this integrated active-passive device are also shown as insets in Figure F1. Signals entering ports A and A' control the transmission of signals entering the B port.

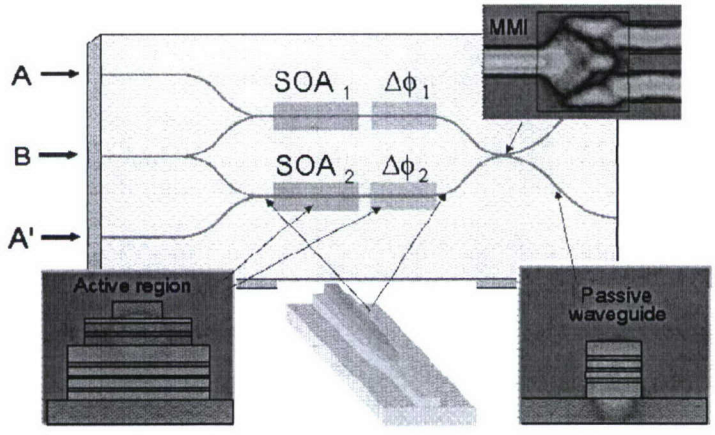

Figure F1: Schematic of an integrated SOA-based nonlinear Mach-Zehnder interferometer. Insets show designs and optical mode simulations of the individual components.

For operation at data bit rates greater than 100 Gb/s the ultrafast carrier dynamics of the SOA's play a crucial role. Patterning effects due to carrier population dynamics with recovery times on the order of 100ps need to be minimized or compensated for. Ultrafast nonequilibrium dynamics that take place on a sub-picosecond timescale begin to play a role [3]. To analyze these effects and optimize the design and functionality of these devices, we need to study both the index of refraction changes and gain/loss changes that occur in various materials and device structures

with femtosecond time resolution and with a variety of wavelength combinations [4]. To that end we have developed a two-color heterodyne [5] pump-probe approach for femtosecond studies in the 1.5μm wavelength regime. Figure F2 shows the experimental setup for this approach.

In this schematic, the150-fs pulse optical signal centered at 1.53um from the output of a synchronously pumped optical parametric oscillator (OPO) is divided into two paths, the pump and the probe. The probe beam passed through a highly nonlinear bismuth-oxide fiber [6]. The output signal from this fiber consists of a broad chirped optical-spectrum centered at 1.53um in frequency domain, while in the time domain, the pulsewidth is larger than the initial 150fs at the output of the OPO. This signal is then passed through a bandpass filter (BPF) centered at 1560nm, and passed through a grating pair to remove the chirp and shorten the pulsewidth back to 150fs. This signal is divided once again into two paths, one of which (probe) is frequency shifted by 40 MHz with an acousto-optic modulator (AOM) and is incident upon the device under test (DUT), while the other (ref) is frequency shifted by 39 MHz and is passed around the DUT.

In the pump path, the original signal is passed through a translation stage which is controlled by a computer to change the time delay between the pump and the probe, and is then subsequently chopped and directed to the DUT. The output signal from the DUT consisting of the both the pump and the probe signals at two different wavelengths is passed through a BPF centered at 1560 nm to remove the pump signal. The probe signal and the reference signal are then combined and detected using a photodiode. The output of the photodiode consists of the beat signal between the probe and Ref signals at 1MHz frequency which in turn is detected by the receiver and its amplitude and phase is measured using a lock-in amplifier. Using this method we can study both gain and index of refraction changes as a function of time.

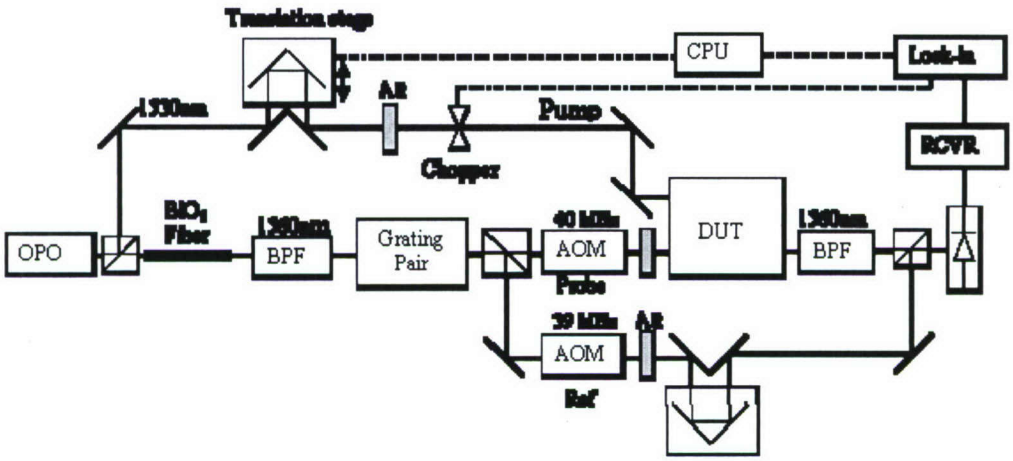

Figure F2: Schematic of heterodyne, two-color femtosecond pump-probe apparatus

In addition to the above studies, we are also employing a two-color pump probe at 800nm pump and 1550nm probe for investigations of ultrafast dynamics in SiGe saturable absorber mirrors and ion implanted Si devices.

References:

1. R. P. Schreieck, M. H. Kwakernaak, H. Jackel, and Hans Melchior, "All-optical switching at Multi-100Gb/s data rates with Mach-Zehnder interferometer switches", IEEE J. Quant. Electron., 38, 1053-1061, 2002.
2. K. E. Stubkjaer, "Semiconductor optical amplifier-based all-optical gates for high-speed optical processing," IEEE J. Sel. Top. In Quant. Electron., 6, 1428-1435, 2000.
3. K.L. Hall, E.R. Thoen and E.P. Ippen,, "Nonlinearities in Active Media, Semiconductors and Semimetals," Chapter 2, Vol 59, Eds. E. Garmire and A. Kost, Academic Press, 1998.

4. T. Katayama, H. Kawaguchi, "Measurement of self- and cross-gain saturation dynamics using two-color heterodyne pump-probe technique", IEEE Photonics Tech. Lett., 17, 1244-1246, 2005.
5. K.L. Hall, G. Lenz, E.P. Ippen, and G. Raybon, "Heterodyne Pump-Probe Technique for Time-Domain Studies of Optical Nonlinearities in Waveguides," Optics Lett. 17, pp. 874-876, 1992
6. J. T. Gopinath, H. M. Shen, H. Sotobayashi, E. P. Ippen, T. Hasegawa, T. Nagashima, N. Sugimoto, "Highly Nonlinear Bismuth-Oxide Fiber for Smooth Supercontinuum Generation at 1.5 μm," Opt. Express,12, p.5697-5702, 2004.

G: Continuum Generation in Photonic Crystal Fibers for OCT

The high cost and complexity of femtosecond laser sources has driven the development of lower cost alternatives for ultrahigh resolution optical coherent tomography (OCT) imaging. Among them, continuum generation in highly nonlinear fibers is one of the promising techniques. Photonic crystal fiber (PCF) technology is extremely powerful because it enables customization of the fiber dispersion profile, which can be used to control the nonlinear processes responsible for continuum generation. The realization of supercontinuum generation in PCF [1] has enabled ultrahigh resolution OCT at wavelengths throughout the visible and near infrared [2-4].

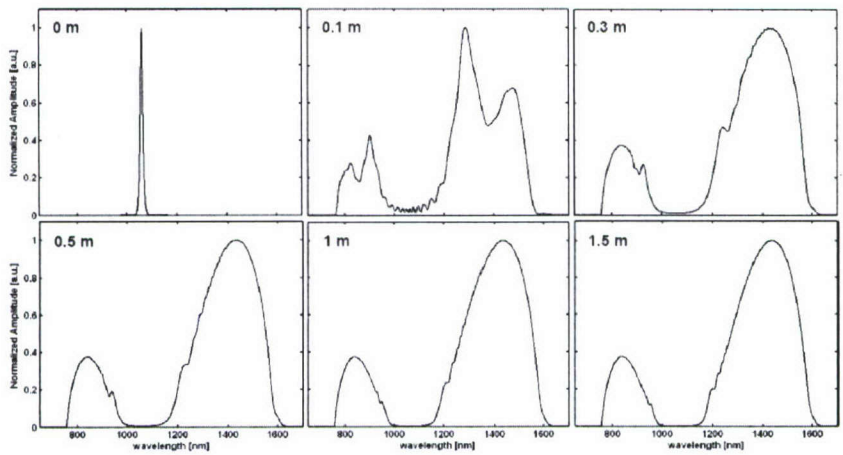

Figure G1. Simulated fiber length dependence of the continuum spectrum generated by 85 fs, 18 kW peak power pulses at 1060 nm. Nearly complete depletion of the pump wavelength is observed along with creation of two high brightness main peaks centered near 800 nm and 1300 nm.

We have developed a novel PCF design concept for a broadband, stable continuum light source for ultrahigh resolution OCT imaging [5]. By injecting pulses at 1064 nm from a Nd:Glass laser into a commercially available photonic crystal fiber with a parabolic dispersion profiles and two closely spaced zero dispersion points centered around 1050 nm, we numerically and experimentally demonstrate that a stable continuum can be generated with high brightness double peaks centered at 800 nm and 1300 nm, two primary wavelengths of interest to the OCT imaging community.

Fig. G1 presents numerical results for the length dependence of the continuum, with spectra displayed on a linear scale. The fact that the continuum rapidly evolves into a double peak structure with nearly complete depletion of the pump wavelength predicts that the main spectral peaks can be localized to the important OCT imaging wavelength regions near 800 nm and 1300 nm. The input spectrum is rapidly broadened within 10 cm to a full spectral width of more than one octave between 700 nm and 1500 nm. Additional propagation in the fiber leads to further depletion of the region between the two spectral peaks as well as filling in and smoothing of the main peaks.

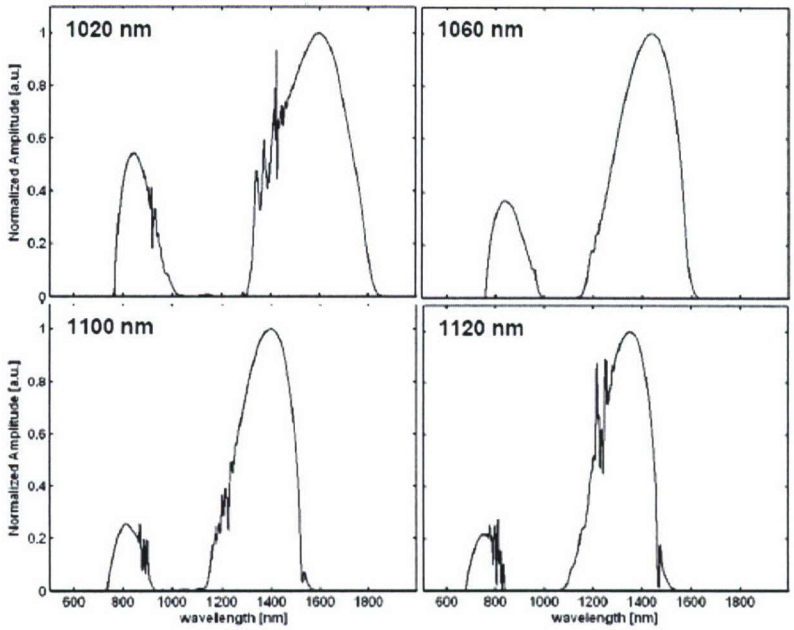

Figure G2. Simulated pump wavelength dependence for optimal continuum generation. Input pulses of 85 fs, 18 kW peak power illustrate differences in continuum as a function of pump wavelength.

Fig. G2 presents spectra resulting from simulations of 85 fs, 18 kW peak power pulses propagated through a 2 m length of the photonic crystal fiber at various center wavelengths around the depletion region. For OCT imaging, spectral shape is a critical determinant of image quality since non-Gaussian spectra with large modulation can lead to large coherence wings on the interference point spread function [6]. The simulations indicate that smooth, twin peak spectra can be achieved when the wavelength of the pump pulse is located between the two zero dispersion wavelengths. Since choosing the optimal pump wavelength is largely equivalent to optimizing the fiber dispersion profile for a fixed pump wavelength, custom photonic crystal design and fabrication should enable ultrahigh resolution OCT with several commercially available femtosecond oscillators.

The measured continuum spectrum (the solid line) and the pump spectrum (the dashed line) are presented in Fig. G3. The continuum spectrum shown is a concatenation of spectra measured separately with 0.5 nm resolution, a method which enables more precise representation of spectral shape and relative amplitude. The spectrum agrees reasonably well with previously presented simulation results. As predicted in the simulation, energy is efficiently depleted from the pump wavelength and transferred to the two spectral bands around 800 nm and 1300 nm. Bandwidths of 156 nm and 116 nm are achieved at 1300 nm and 800 nm, respectively. However, the modulation seen on the spectrum is greater than expected based on numerical simulations for an injected pulse at 1064 nm. Error in the approximation of the higher order dispersion terms for the fiber, the change in the fiber's dispersion profile over the length and coupling effect may be the causes for the spectral modulation.

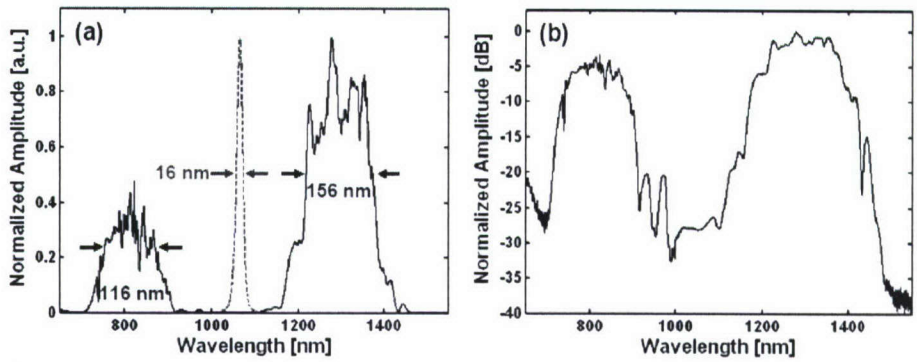

Figure G3. Experimental measurement of continuum spectrum on (a) linear and (b) log scales. The pump laser spectrum is also shown in (a). These spectra are created from concatenation of individually measured spectra in the 800 nm and 1300 nm wavelength regions.

Figure G4 shows the recorded RF noise spectra acquired using a fast photodiode. The measurements were made at the first harmonic of the laser repetition rate and normalized to the carrier power. Detected first harmonic carrier power was 1.13 dBm for the oscillator alone and -22.97 dBm and -17.0 dBm for the wavelength regions of 800 nm and 1300 nm, respectively. The noise spectra largely tracks that of the oscillator alone implying that OCT imaging can be performed with high sensitivity due to the lack of excess amplitude noise.

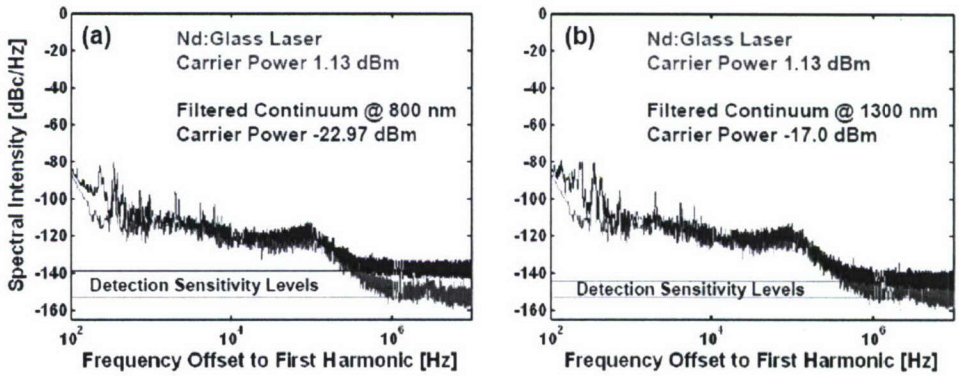

Figure G4. Experimental measurement of RF noise spectra for the filtered wavelength regions around (a) 800 nm and (b) 1300 nm. The noise spectra are compared to the RF spectrum for the Nd:Glass oscillator alone.

The continuum spectrum was used with time-domain, ultrahigh resolution OCT systems to demonstrate imaging in biological tissue. It should be noted that, while these sources were demonstrated for time-domain ultrahigh resolution OCT imaging, they can also be implemented with spectrometer based spectral domain OCT systems for high speed, ultrahigh resolution OCT at 800 nm and 1300 nm [7-10]. System performance characterization is presented for both 800 nm and 1300 nm in Fig. G5. Figures 5(a) and (b) compares the point spread function on a linear scale for both wavelengths while (c) and (d) presents the same data on a logarithmic scale. At 800 nm, 3.0 μm full width at half maximum (FWHM) is achieved, which for index of refraction in tissue of 1.38 will provide ~ 2.2 μm in tissue. At 1300 nm, 6.5 μm FWHM provides ~ 4.7 μm in tissue. The sidelobe coherence artifacts on the point spread functions at both wavelengths are present at ~ 25-30 dB, indicating further work to investigate spectral smoothing in the PCF will be important for performance improvement since sidelobe levels of 40-50 dB are desirable for OCT imaging. Sensitivity was measured to be ~ -103 dB for 1.0 mW sample exposure at 800 nm and ~ -107 dB for 3.0 mW sample exposure at 1300 nm.

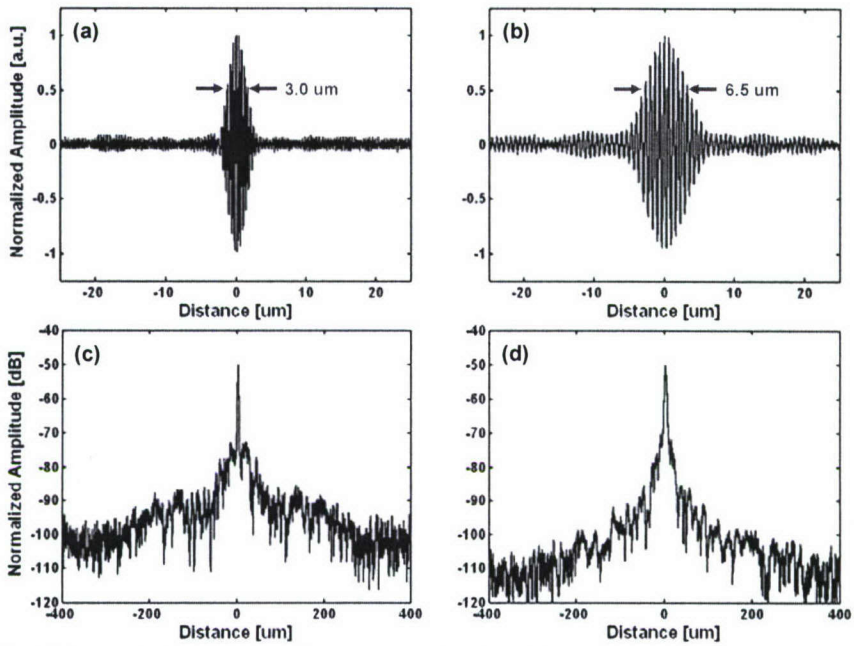

Figure G5. Ultrahigh resolution OCT performance evaluation. Linear (a,b) and logarithmic (c,d) point spread functions are shown for both 800 nm (a,c) and 1300 nm (b,d).

Fig. G6 presents representative OCT imaging results in formalin fixed hamster cheek pouch at 800 nm and 1300 nm. Fine features such as the epithelium (e), connective tissue (c), and muscular layers (m) in the fixed tissue specimen can be visualized with high resolution and high contrast. Some blurring of the images results from the sidelobe coherence artifact, but this can be improved with further optimization of the continuum light source.

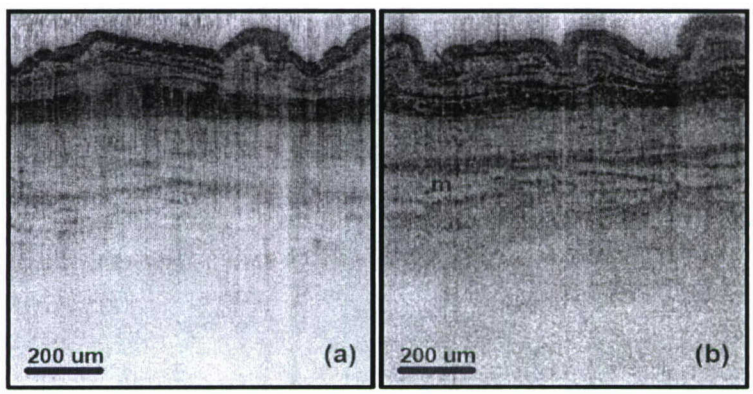

Figure G6. Ultrahigh resolution OCT images of formalin fixed hamster cheek pouch at (a) 800 nm and (b) 1300 nm. Enhanced image penetration is noticeable at 1300 nm and important features such as the epithelium (e), connective tissue bands (c), and muscular layers (m) can be distinguished.

While it is unlikely that continuum generation sources will find widespread use for ultrahigh resolution retinal imaging at 800 nm due to the availability of broadband superluminescent diode (SLD) sources, they offer a very promising alternative to SLD's for ultrahigh resolution imaging in other applications where more power and/or longer wavelengths are required. The novel PCF design with two closely spaced zero dispersion wavelengths offers a solution to the problems of excess noise and low power efficiency that have hindered the use of supercontinuum generation for ultrahigh resolution OCT in the 1300 nm wavelength range. The work also suggests that a single commercially available oscillator combined with various highly nonlinear fibers can be used

to generate stable, high brightness spectra for ultrahigh resolution OCT imaging throughout the near infrared wavelength region.

References

[1] J. K. Ranka, R. S. Windeler, and A. J. Stentz, "Visible continuum generation in air-silica microstructure optical fibers with anomalous dispersion at 800 nm," *Optics Letters* 25(1): 25-27 (2000).

[2] I. Hartl, X. D. Li, C. Chudoba, R. K. Hganta, T. H. Ko, J. G. Fujimoto, J. K. Ranka, and R. S. Windeler, "Ultrahigh-resolution optical coherence tomography using continuum generation in an air-silica microstructure optical fiber," *Optics Letters* 26(9): 608-10 (2001).

[3] B. Povazay, K. Bizheva, A. Unterhuber, B. Hermann, H. Sattmann, A. F. Fercher, W. Drexler, A. Apolonski, W. J. Wadsworth, J. C. Knight, P. S. J. Russell, M. Vetterlein, and E. Scherzer, "Submicrometer axial resolution optical coherence tomography," *Optics Letters* 27(20): 1800-2 (2002).

[4] W. Drexler, "Ultrahigh-resolution optical coherence tomography," *Journal of Biomedical Optics* 9(1): 47-74 (2004).

[5] A. D. Aguirre, N. Nishizawa, J. G. Fujimoto, W. Seitz, M. Lederer, and D. Kopf, "Continuum generation in a novel photonic crystal fiber for ultrahigh resolution optical coherence tomography at 800 nm and 1300 nm," *Optics Express* 14(3): 1145-60 (2006).

[6] S. R. Chinn and E. A. Swanson, "Blindness Limitations in Optical Coherence Domain Reflectometry," *Electronics Letters* 29(23): 2025-27 (1993).

[7] M. Wojtkowski, T. Bajraszewski, P. Targowski, and A. Kowalczyk, "Real-time in vivo imaging by high-speed spectral optical coherence tomography," *Optics Letters* 28(19): 1745-47 (2003).

[8] M. Wojtkowski, V. J. Srinivasan, T. H. Ko, J. G. Fujimoto, A. Kowalczyk, and J. S. Duker, "Ultrahigh-resolution, high-speed, Fourier domain optical coherence tomography and methods for dispersion compensation," *Optics Express* 12(11): 2404-22 (2004).

[9] N. Nassif, B. Cense, B. H. Park, S. H. Yun, T. C. Chen, B. E. Bouma, G. J. Tearney, and J. F. de Boer, "In vivo human retinal imaging by ultrahigh-speed spectral domain optical coherence tomography," *Opt Lett* 29(5): 480-2 (2004).

[10] S. H. Yun, G. J. Tearney, B. E. Bouma, B. H. Park, and J. F. de Boer, "High-speed spectral-domain optical coherence tomography at 1.3 mu m wavelength," *Optics Express* 11(26): 3598-604 (2003).

H: Frequency Swept Lasers and Fourier Domain Mode Locking (FDML)

Femtosecond lasers have found various applications as high performance light sources for biomedical imaging. Besides the use of their high pulse powers for non-linear imaging, their broad spectrum and short coherence length served as enabling tools for ultrahigh resolution optical coherence tomography [1-3]. Recently, efforts have been made to apply narrowband, rapidly tunable narrowband continuous wave lasers for OCT imaging to achieve higher acquisition speeds and sensitivity [4-15]. This concept is called "swept source OCT," or sometimes "optical frequency domain imaging (OFDI)." The measurement concept is similar to optical frequency domain reflectometry (OFDR), although the requirements for the laser are very different in OCT applications.

To be suitable for OCT imaging, a laser at 1300 nm wavelength, with 100 nm or more tuning range, 0.1 nm or less instantaneous linewidth and 50,000 – 500,000 sweeps per second is desired [14]. The resulting frequency sweep rates are up to 10^{19} Hz/s, and the required average output power is >10 mW.

In order to understand the operation, describe the dynamics, and investigate limitations of such rapidly tuned lasers, a high speed, frequency swept laser light source at 1300 nm was developed. The laser uses a fiber ring design with an additional booster amplifier. Details of the setup are

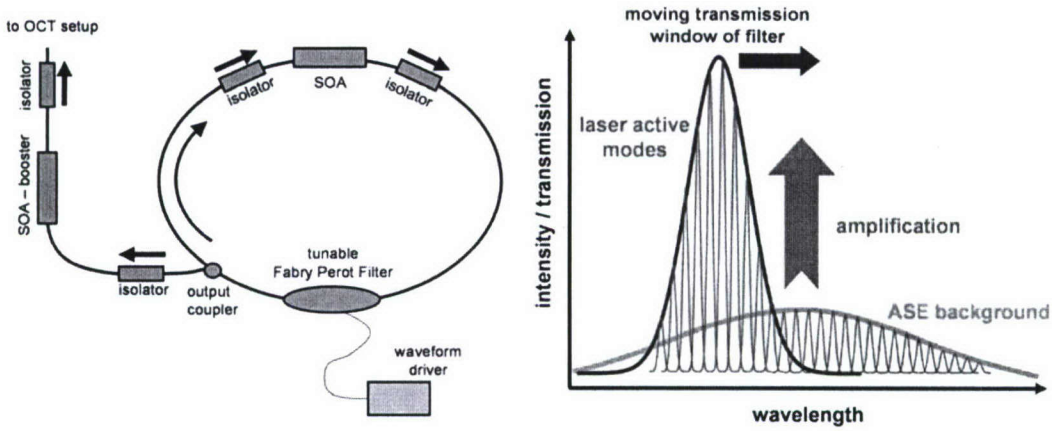

Figure H1. Left: Schematic of the amplified frequency swept laser source. The laser uses a fiber coupled semiconductor amplifier and a tunable fiber Fabry-Perot-filter. An extracavity semiconductor amplifier boosts the laser output. Right: Concept of cavity tuning: build up of laser activity from ASE background.

described in ref. [12]. To assist in optimization of the swept laser performance, a theoretical model was developed for the dynamic operation of swept laser sources [12]. The following discussion addresses the fundamental limitation of standard cavity-tuned lasers. In cavity-tuning, the maximum tuning speed is usually limited by the time-constant of the laser to build up lasing from the amplified stimulated emission (ASE) background. This time constant is dependent on the filter function, the ASE intensity, the saturation power, the laser gain and the cavity roundtrip time. In the following analysis we consider two distinct limits, which characterize the frequency tuning behavior of the frequency swept laser source: *(i) the saturation limit and (ii) the single roundtrip limit*.

The first limit or characteristic frequency at which a change in the laser dynamics can be expected is the "saturation limit". This limit represents the maximum frequency tuning speed which still allows for full build-up of lasing activity from the ASE background. Fig. H1 (right) shows the concept for estimating this characteristic frequency. We assume a background intensity of ASE from the laser medium. The broad green curve shows the ASE spectrum of the laser gain medium, with a characteristic mode structure inside a cavity (narrow green curves). When the filter window is tuned in wavelength, the ASE background is amplified up to the saturation power limit of the gain medium, provided that the time the filter transmits the given wavelength is enough for this build up

With typical experimental parameters the estimated sweep speed is ~11,600 Hz for the presented ring laser. This value represents a rough estimate of how fast the laser can be tuned while preserving the maximum power output. Shorter cavities, long duty cycles and linear scans will enable higher speeds. Experimentally it was observed that tuning from shorter to longer wavelengths (i.e. to lower energy or frequency) is favored compared to tuning in the opposite direction. This effect can be related to nonlinear effects and carrier dynamics in the semiconductor gain medium. This assists the tuning process because the lasing does not have be build up solely from ASE.

For frequency sweep speeds higher than the "saturation limit", the output power will decrease until it reaches the "single roundtrip limit", the frequency tuning speed above which the light on the average makes only one pass from the gain medium to the filter and is coupled out. The filter has tuned so rapidly that during the next roundtrip it already blocks the wavelength. The output light shows the characteristics of ASE which is spectrally filtered and amplified once (on the average. With the parameters of the experimental setup, the sweep frequency for the single round trip limit is f_{single} is 30,700 Hz. This limit represents an estimate of the maximum frequency

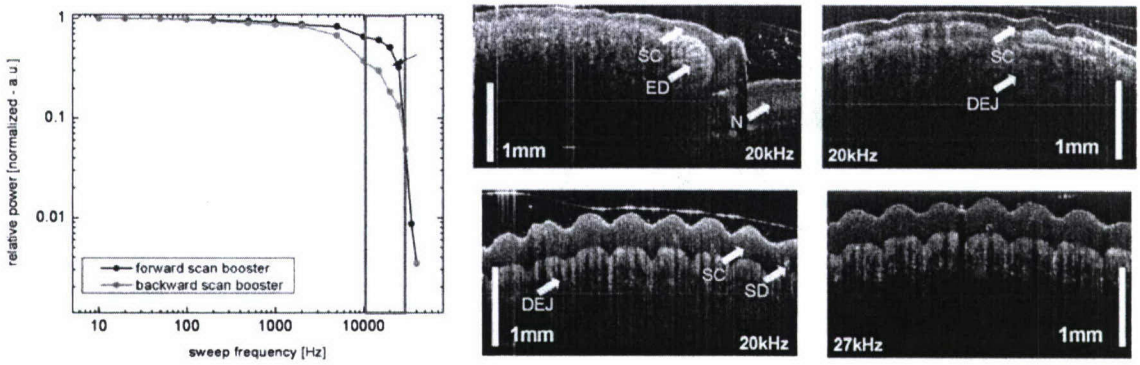

Figure H2. Left: Output power vs. sweep frequency. Right: Imaging examples.

for which laser feedback can occur. When the laser is frequency swept above this speed, it operates like a post-filtered broadband light source rather than a tuned cavity.

Fig. H2 (left) shows the output power of the laser for different drive frequencies of the filter. The plots give the power values for the forward sweeps (blue) and the backward sweeps (green). The values are normalized to the output power in non-swept operation. The rectangle marks the region between saturation limit and single roundtrip limit. It can be seen that up to the saturation limit, the power stays almost constant and begins to drop when tuning frequencies exceed the saturation limit. The power falls off completely when the single roundtrip limit is approached. No laser operation is possible above the single roundtrip limit. Due to the saturation limit and the single roundtrip limit, high quality imaging was restricted to drive frequencies of 20 kHz (with a unidirectional filter sweep) or 10 kHz (with a bidirectional filter sweep). In both cases the resulting line rate in OCT applications is limited to about 20 kHz for high quality images. These effects represent a fundamental limit in standard tunable lasers. Concepts for shifting the optical frequency inside the laser cavity, such as the use of acousto-optic or electro-optic frequency shifters, during the roundtrip can usually not provide sufficient shifting to support the desired tuning rates because these devices typically do not generate shifts larger than a few GHz.

The only solution to increase the tuning speed in standard tunable lasers is to decrease the cavity length and build a shorter resonator.. A completely different and more elegant solution that entirely overcomes the previously-described speed limitations and simultaneously improves many other performance aspects of the swept source is the concept of Fourier Domain Mode Locking (FDML).

Fourier Domain Mode Locking (FDML) is a new technique designed to overcome limitations in the maximum tuning speed of swept laser sources and to generate a spectrally very clean frequency sweep – equivalent to train of highly chirped laser pulses [16 - 19]. Fig. H3 is a schematic showing the concept of an FDML laser compared to a standard frequency-swept laser. In a standard frequency-swept laser, light from a broadband gain medium is spectrally filtered by a narrowband optical bandpass filter within the cavity and fed back to the gain medium.

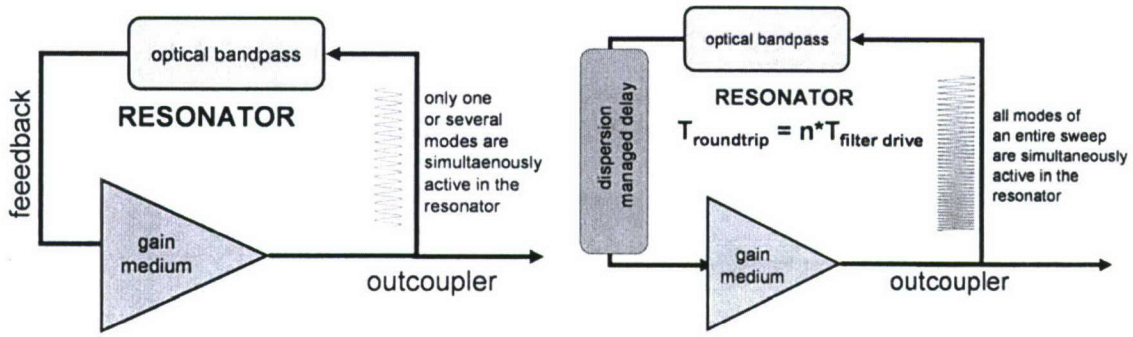

Figure H3. Left: Standard tunable laser. Right: Fourier domain mode locking (FDML). The tunable optical bandpass filter is periodically driven with a period matched to the round-trip time of the cavity or a harmonic.

In the standard swept laser, only longitudinal modes with frequencies that are transmitted through the narrowband optical filter can lase. When the center frequency of the narrowband optical filter is tuned during a frequency sweep, lasing must build up from spontaneous emission at each new frequency position of the filter. This significantly limits the performance of high-speed, frequency-swept lasers, imposing a trade-off between the speed of the frequency sweep versus linewidth, output power, and tuning range [12].

In FDML lasers, a dispersion managed delay line is incorporated into the laser cavity and the narrowband optical filter is tuned periodically at the cavity round-trip time, or a harmonic of the round-trip time (Fig. H3 (right)). This produces a quasi-stationary mode of operation. Light from one frequency sweep propagates through the cavity and returns to the filter at the exact time when the transmission window of the optical bandpass filter is tuned to the same optical frequency. Therefore, light from the previous round-trip is coupled back to the gain medium and lasing does not have to build up from spontaneous emission. In other words, an entire frequency sweep is optically stored within the dispersion managed delay line in the laser cavity. Under ideal operation, sequential frequency sweeps have the same phase evolution and are mutually coherent. The narrowband optical bandpass filter dissipates almost no energy because the backcoupled light contains only frequencies that are matched to the transmission window filter at each moment. In the frequency domain, this requires destructive interference of all longitudinal modes that are not transmitted through the narrowband filter at a given time. Thus, the phases of the longitudinal modes must be locked. Standard mode-locked lasers have longitudinal modes locked with constant phase, which corresponds to the generation of a train of short pulses at a repetition rate equal to the cavity round-trip time. Fourier domain mode-locked lasers have modes locked with a different phase relationship. The laser output is not a train of short pulses; instead, it is a train of frequency sweeps or highly chirped, very long pulses. The tunable narrowband filtering is equivalent to an infinite number of narrowband amplitude modulators that are slightly out of phase. Fourier domain mode locking is performed by periodic spectral modulation, rather than amplitude modulation. This can be viewed as the Fourier domain analog of mode locking for short-pulse generation.

Fig. H4 is a schematic diagram of the FDML laser. The laser is based on a fiber-ring geometry with a semiconductor optical amplifier (SOA from InPhenix, Inc.) as a gain medium and a fiber Fabry-Perot filter (FFP-TF, Micron Optics, Inc.) as the tunable, narrowband optical bandpass filter. The SOA is polarization insensitive with a polarization dependent gain of ~0.5 dB. The fiber Fabry Perot tunable filter has a free spectral range of ~200 nm at a center wavelength of 1300 nm and a finesse of ~800. The waveform driver for the fiber Fabry-Perot consists of a digital function generator and an electric power amplifier for driving the low-impedance ~2.2 μF capacitive load of the fiber Fabry-Perot lead zirconate titanate (PZT) actuator. With respect to thermal stability, the drift of the resonance frequency caused by temperature variations as well as drift in the PZT bias offset were minimal and a manual adjustment after about 15 minutes warm up time ensured stable operation for many hours.

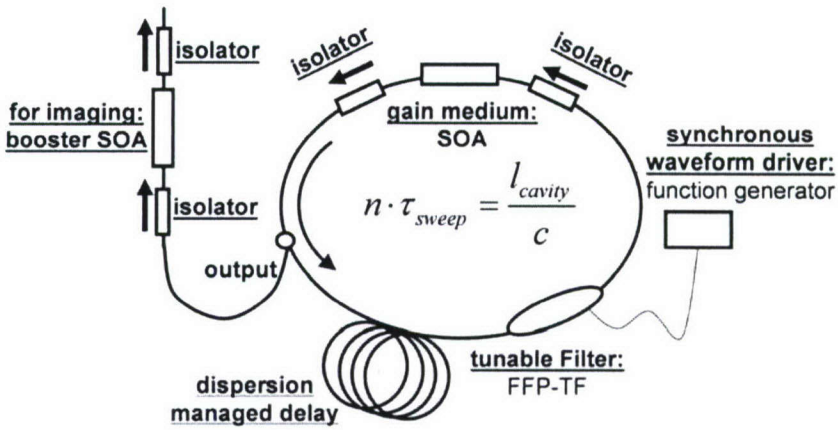

Figure H4. Schematic diagram of the Fourier domain mode-locked (FDML), high-speed, frequency-swept laser.

The optical isolators eliminate extraneous intracavity reflections and ensure unidirectional lasing of the ring cavity. A 30% fiber splitter acts as the output coupler. After isolation, the laser output is amplified with a second fiber-coupled semiconductor amplifier (SOA from InPhenix, Inc.), which functions as a booster amplifier. The booster SOA is also polarization insensitive, with a polarization dependent gain of about 0.5 dB. The losses throughout the cavity are typically 0.35 dB for each isolator, <2 dB for the fiber Fabry-Perot filter, 1.8 dB for the 30 % output coupler and 2.2 dB, 1.5 dB and 1 dB for 7 km, 4.8 km and 3.3 km lengths of fiber, respectively. Between -5 dB and -7 dB of the output of the SOA are coupled back into the SOA. The fiber-to-fiber small signal gain of the SOA is 20 dB.

Fig. H5 shows the transient intensity profiles of the frequency-swept laser for forward (shorter to longer wavelengths) and backward (longer to shorter wavelengths) frequency sweeps at different effective sweep rates. The data is shown for the direct laser output without post-amplification in order to ensure that the transient intensity profiles are not obscured or shaped by saturation effects. The physical cavity length was 7 km, which corresponds to a 10-km optical path length. Resonances in the tunable filter drive frequency were observed at 29 kHz and at the higher harmonics. Because two frequency sweeps, one forward and one backward, were generated for each sinusoidal drive cycle, a 29 kHz filter drive frequency corresponds to an effective sweep rate of 58 kHz. In contrast to other high-speed, frequency-swept lasers, in FDML lasers, the forward and backward frequency sweeps have the same intensity profile and the same maximum power.

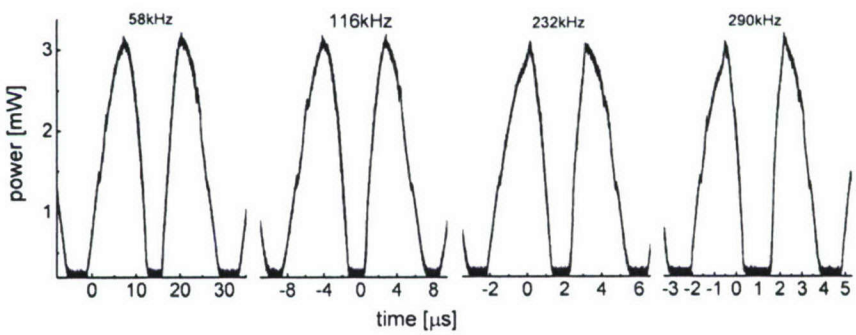

Figure H5. Transient intensity profiles of the FDML laser for different effective sweep rates. The traces always show the transient intensity for one forward and one backward frequency sweep.

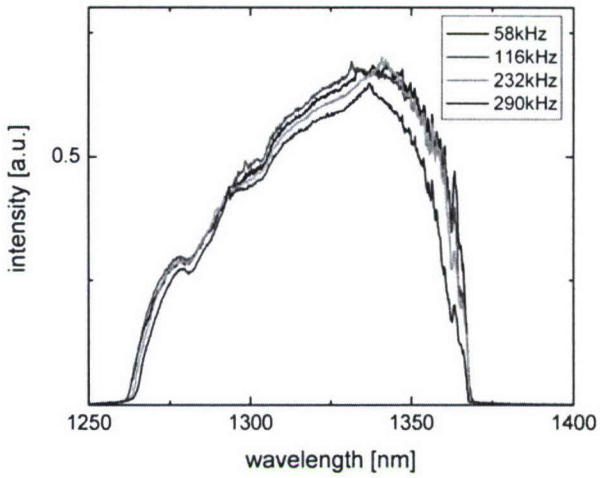

Figure H6. Integrated spectra of the FDML source for different effective sweep rates.

Fig. H5 shows that neither the shape, nor the amplitude of the transient intensity profiles changes as the filter drive frequency is increased. The maximum filter drive frequency and frequency sweep rate (change of the optical frequency per time) are only limited by the mechanical response of the tunable narrowband optical filter. This enables very high-speed OCT imaging, as demonstrated in the following subsections. Fig. H6 shows the integrated spectral output of the source and again no sweep frequency dependence can be observed. Fig. H7 (top) shows the RF fringe signals from a Michelson interferometer for the case of an FDML and a standard swept laser. As expected, the mutual coherent sweeps in the FDML case provide superior phase stability. The roll off characteristic of the point spread functions in OCT application (Fig. H7 (bottom) reflects the instantaneous linewidth or coherence length.

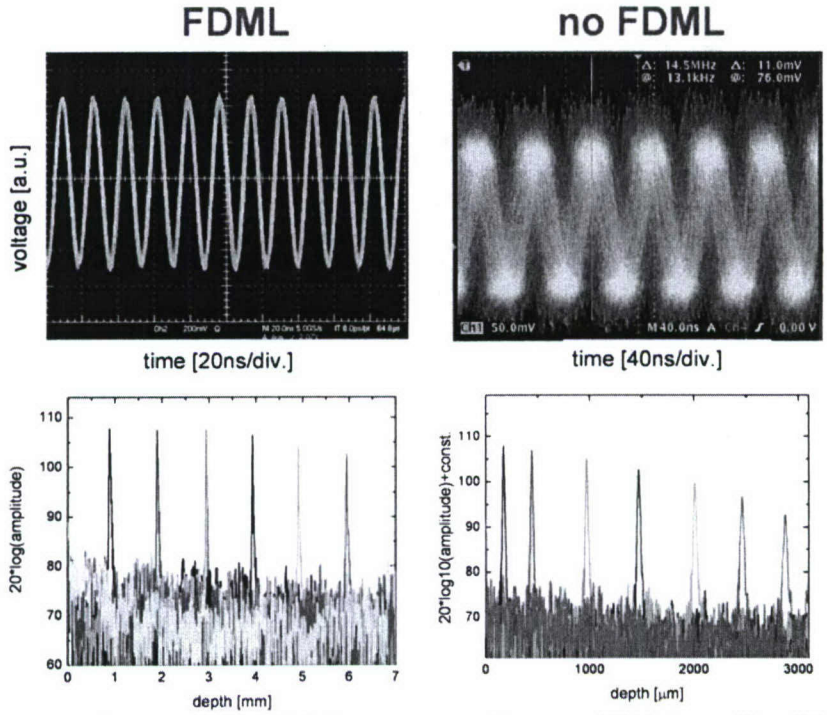

Figure H7. Superior performance of a FDML laser compared to a non-FDML laser. Top: FDML lasers show much higher phase stability of the RF fringe signals in OCT applications. Bottom: The instantaneous linewidth of FDML lasers is much narrower and the instantaneous coherence length much longer than that of a comparable standard swept laser. The result is a much slower roll off in the point spread functions in OCT application for the case of a FDML laser.

Again the superior performance of FDML lasers is evident, up to 7 mm ranging is possible whereas in the comparable standard lasers a considerable decrease over 3 mm can be observed. From the coherence length a linewidth of 0.06nm can be calculated, which is much narrower than the filter width of about 0.25 nm. This important result underlines the fact that in FDML the linewidth is decoupled from the filter width, similar to non-swept lasers. Much broader spectral filters can therefore be applied, reducing component costs and reducing losses in the cavity.

The application of the frequency-swept FDML laser for high-speed, swept-source OCT imaging is shown in the images of Fig. H8. The images of a human finger *in vivo* are acquired at a sweep rate of 40 kHz. Compared to the images acquired with a non FDML laser (see section 1) these images exhibit superior background levels, contrast, and noise performance. No artifacts in the form of stripe like structures can be seen, the images have an extremely clean appearance, and penetration well into the dermis is apparent.

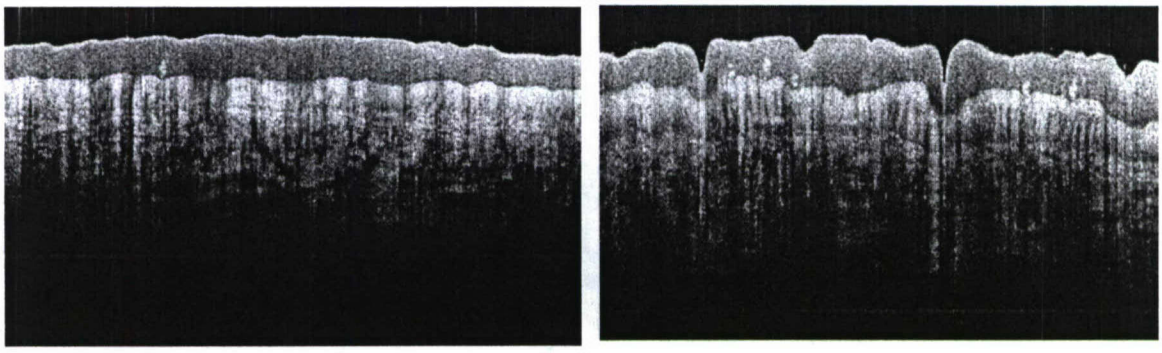

Figure H8. OCT images acquired with FDML laser; images of human finger *in vivo*.

References

[1] D. Huang, E. A. Swanson, C. P. Lin, J. S. Schuman, W. G. Stinson, W. Chang, M. R. Hee, T. Flotte, K. Gregory, C. A. Puliafito, and J. G. Fujimoto, "Optical coherence tomography," *Science* 254(5035): 1178-81 (1991).

[2] W. Drexler, U. Morgner, R. K. Ghanta, F. X. Kärtner, J. S. Schuman, and J. G. Fujimoto, "Ultrahigh-resolution ophthalmic optical coherence tomography," *Nature Medicine* 7(4): 502-07 (2001).

[3] W. Drexler, U. Morgner, F. X. Kartner, C. Pitris, S. A. Boppart, X. D. Li, E. P. Ippen, and J. G. Fujimoto, "In vivo ultrahigh-resolution optical coherence tomography," *Optics Letters* 24(17): 1221-23 (1999).

[4] A. F. Fercher, C. K. Hitzenberger, G. Kamp, and S. Y. Elzaiat, "Measurement of Intraocular Distances by Backscattering Spectral Interferometry," *Optics Communications* 117(1-2): 43-48 (1995).

[5] F. Lexer, C. K. Hitzenberger, A. F. Fercher, and M. Kulhavy, "Wavelength-tuning interferometry of intraocular distances," *Applied Optics* 36(25): 6548-53 (1997).

[6] B. Golubovic, B. E. Bouma, G. J. Tearney, and J. G. Fujimoto, "Optical frequency-domain reflectometry using rapid wavelength tuning of a Cr4+:forsterite laser," *Optics Letters* 22(22): 1704-06 (1997).

[7] S. R. Chinn, E. A. Swanson, and J. G. Fujimoto, "Optical coherence tomography using a frequency-tunable optical source," *Optics Letters* 22(5): 340-2 (1997).

[8] S. H. Yun, C. Boudoux, G. J. Tearney, and B. E. Bouma, "High-speed wavelength-swept semiconductor laser with a polygon-scanner-based wavelength filter," *Optics Letters* 28(20): 1981-83 (2003).
[9] M. A. Choma, M. V. Sarunic, C. H. Yang, and J. A. Izatt, "Sensitivity advantage of swept source and Fourier domain optical coherence tomography," *Optics Express* 11(18): 2183-89 (2003).
[10] S. H. Yun, G. J. Tearney, J. F. de Boer, N. Iftimia, and B. E. Bouma, "High-speed optical frequency-domain imaging," *Optics Express* 11(22): 2953-63 (2003).
[11] M. A. Choma, K. Hsu, and J. Izatt, "Swept source optical coherence tomography using an all-fiber 1300-nm ring laser source," *Journal of Biomedical Optics* 10(4): #044009 (2005).
[12] R. Huber, M. Wojtkowski, K. Taira, J. G. Fujimoto, and K. Hsu, "Amplified, frequency swept lasers for frequency domain reflectometry and OCT imaging: design and scaling principles," *Optics Express* 13(9): 3513-28 (2005).
[13] J. Zhang and Z. P. Chen, "In vivo blood flow imaging by a swept laser source based Fourier domain optical Doppler tomography," *Optics Express* 13(19): 7449-57 (2005).
[14] R. Huber, M. Wojtkowski, J. G. Fujimoto, J. Y. Jiang, and A. E. Cable, "Three-dimensional and C-mode OCT imaging with a compact, frequency swept laser source at 1300 nm," *Optics Express* 13(26): 10523-38 (2005).
[15] Y. Yasuno, V. D. Madjarova, S. Makita, M. Akiba, A. Morosawa, C. Chong, T. Sakai, K. P. Chan, M. Itoh, and T. Yatagai, "Three-dimensional and high-speed swept-source optical coherence tomography for in vivo investigation of human anterior eye segments," *Optics Express* 13(26): 10652-64 (2005).
[16] R. Huber, K. Taira, and J. G. Fujimoto, "Fourier Domain Mode Locking: Overcoming limitations of frequency swept light sources and pulsed lasers," paper presented at Conference on Lasers and Electro-Optics Europe/ European Quantum Electronics Conference (CLEO/Europe - EQEC 2005), Munich, Germany, 2005.
[17] R. Huber, K. Taira, M. Wojtkowski, and J. G. Fujimoto, "Fourier Domain Mode Locked Lasers for OCT imaging at up to 290kHz sweep rates," *Optical Coherence Tomography and Coherence Techniques II*, Munich, Germany, 2005.
[18] R. Huber, K. Taira, M. Wojtkowski, and J. G. Fujimoto, "Fourier domain mode-locked lasers for swept source OCT imaging at up to 290 kHz scan rates," *Coherence Domain Optical Methods and Optical Coherence Tomography in Biomedicine X*, San Jose, CA, 2006.
[19] R. Huber, M. Wojtkowski, and J. G. Fujimoto, "Fourier Domain Mode Locking (FDML): A new laser operating regime and applications for optical coherence tomography," *Optics Express* 14(8): 3225-37 (2006).

I: Physics of X-Ray Generation: The Ehrenfest Theorem and the Single Atom HHG Spectrum

In spite of the existing extensive body of knowledge about high harmonic generation (HHG), the existing theoretical literature offers almost no absolute quantitative data for the expected EUV and x-ray intensities in HHG experiments. The importance of such a prediction cannot be overestimated: It will show whether current experiments are extracting the entire potential in terms of efficiency and performance, it will guide experiments to possibly better setups, and it will show what is the best performance one can ever expect from a HHG based device.

The vast majority of the existing HHG calculations give a qualitative rather than a quantitative picture, and the yields are most often given in arbitrary units. The apparent reason is the lack of a description of the single-atom response that would be both quantitatively accurate and fast to evaluate. Some studies [1-2] solve simultaneously the Maxwell equations and the time dependent Schrödinger equation (TDSE). However quantitative results are still not obtained, presumably because of insufficient numerical accuracy or reduced dimensionality. Others solve the three-dimensional Maxwell equations with the three step model (TSM) describing the medium response

[3]. This approach also does not provide quantitative results, because the usually employed version of the TSM overestimates the HHG photon yield by orders of magnitude [4].

We have developed an excellent analytic approximation for the HHG single atom response spectrum based on an improved formulation of the TSM. The approximation relates to the effective potential picture, where the atom is assumed to be described by a single electron moving in an effective potential:

$$H = -\frac{1}{2}\nabla^2 + V_{eff}(\mathbf{r}) - xE(t). \qquad (1)$$

H is the Hamiltonian, Veff is the effective potential, and E(t) is the laser field. Atomic units are used. The model in Eq. (1) is commonly used in the combined Maxwell-Schrödinger codes [1] and elsewhere in HHG. The accuracy of the analytic approximation is typically better than a couple of tens of percents, as found by comparison to a numerical integration of the TDSE.

The proposed analytic approximation for the high frequency part of the HHG spectrum is based on the TSM. One should distinguish between two cases: Whether the electron is initially in the ground state of V_{eff} or in an excited state. The latter case is especially important if Veff describes a many-electron atom, because then the highest occupied orbital of the ground state is technically an excited state of V_{eff}. In argon, for example, it would be a 3p state. In addition, one can be simply interested in modeling an experiment where the initial state is an excited atomic state.

If the electron is initially in the ground state of V_{eff} , the standard TSM can be considerably improved if the dipole moment of the electron is computed in the acceleration form (employing Ehrenfest's theorem). This essentially amounts to the replacement of the TSM recombination amplitude by the expression [5]

$$a_{rec}(\mathbf{v}) = -\left\langle 0 \middle| \partial_x V_{eff}(\mathbf{r}) \middle| \mathbf{v} \right\rangle \qquad (2)$$

$|0\rangle$ and $|\mathbf{v}\rangle$ are the ground state and a momentum eigenstate respectively.

When the initial state is an excited state, it can be shown [6] that the TDSE keeps the population of the lower-lying states very small. Projecting the latter out of the momentum eigenstate, the recombination amplitude takes the form [6]

$$a_{rec}(\mathbf{v}) = -\left\langle n \middle| \partial_x V_{eff}(\mathbf{r}) \middle| \mathbf{v} \right\rangle + \sum_{j=1}^{n-1} \left\langle n \middle| \partial_x V_{eff}(\mathbf{r}) \middle| j \right\rangle \left\langle j \middle| \mathbf{v} \right\rangle . \qquad (3)$$

$|n\rangle$ is the initial excited eigenstate of Veff and $|j\rangle$ are all the eigenstates with lower energies.

Figure I1 compares our analytic approximation for the HHG spectrum to numerical solutions of the TDSE. Figure 1a shows the comparison for atomic hydrogen. The low frequency part of the spectrum was computed employing the plasma approximation (see e. g. Eq. (44) in Ref. [4]). To our knowledge, this approximation has not been previously tested in the context of HHG by comparison to the TDSE. Quantitative agreement is demonstrated. Figure 1b demonstrates good agreement for argon, where the Veff we used is the Hartree-Slater potential, similarly to Ref. [1]. Including the last term of Eq. (3) is shown to be crucial.

The improved version of the TSM we suggest here, along with the plasma approximation, combine to a simple analytic formula which reproduces almost the entire HHG spectrum to excellent precision. At least in the context of many applications, such as modeling HHG experiments including optical propagation effects, the problem defined by Eq. (1) can be considered solved analytically to the required precision. This work opens the way to upgrading the existing HHG modeling from the qualitative to the quantitative level.

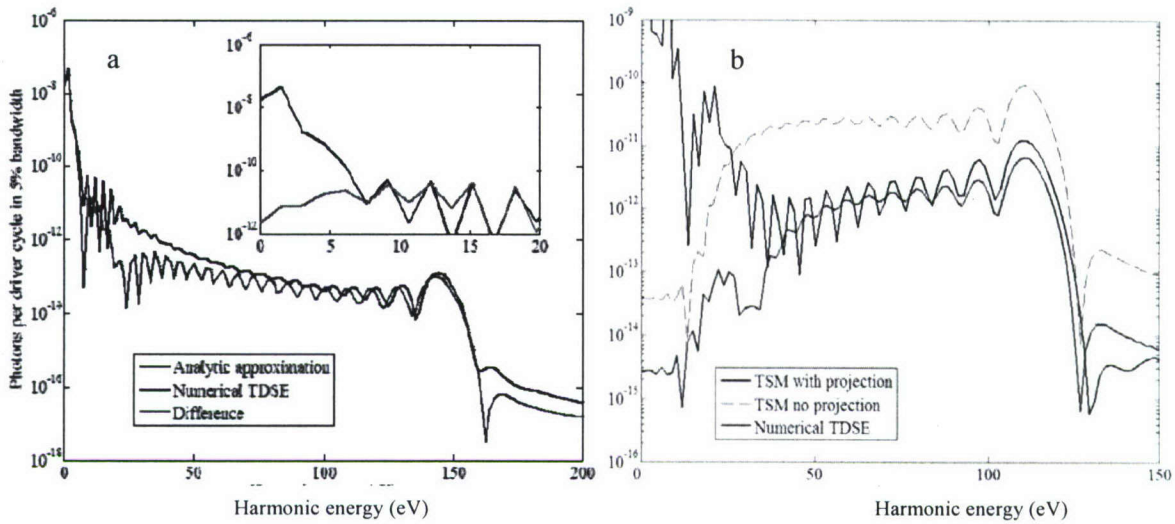

Fig. 1. HHG spectra of a hydrogen (a) and an argon (b) atom in a single cycle 800nm pulse with the amplitudes of 0.14 (a) and 0.12 (b) a.u. Numerical TDSE calculations (black) are compared to analytic approximations (blue). In (a) the plasma approximation was added to the TSM for describing the low frequency part of the spectrum. The red line in the inset shows the spectrum of the error (numerical TDSE minus analytic approximation) at low energies. The dashed line in (b) was calculated omitting the last term in Eq. (3), demonstrating the importance of the latter.

References

[1] N. H. Shon, A. Suda, and K. Midorikawa, Phys. Rev. A 62, 023801 (2000).
[2] M. B. Graade and K. J. Schafer, Phys. Rev. Lett. 89, 213901 (2002).
[3] E. Priori, G. Cerullo, M. Nisoli, S. Stagira, S. De Silvestri, P. Villoresi, L. Poletto, P. Ceccherini, C. Altucci, R. Bruzzese, and C. de Lisio, Phys. Rev. A 61, 063801 (2000).
[4] T. Brabec and F. Krausz, Rev. Mod. Phys. 72, 545 (2000).
[5] A. Gordon and F. X. Kärtner, Phys. Rev. Lett. 95, 223901 (2005).
[6] R. Santra and A. Gordon, Phys. Rev. Lett. 96, 073906 (2006).

J: The Role of Many Electron Effects in High Harmonic Generation

The three step model [1] provides a simple picture of the high harmonic generation (HHG) process in intense laser fields: An electron is ionized and accelerated by the laser field, and then recollides with the parent ion. The vast majority of the models associate the emitted radiation with this one "active" electron alone: The radiation amplitude is typically obtained from the oscillating dipole moment that this one electron creates.

However it is obvious that the bound electrons are disturbed by the electron-ion recollision. The electrostatic field of the recolliding electron must, to some extent, set them into motion. These electrons begin to oscillate, and the oscillation can result in the emission of radiation. Since all noble gases apart from helium have many bound electrons, the contribution of this radiation can be significant. In other words, much of the HHG radiation in heavy noble gases should be emitted by the "inactive" electrons.

We propose [2] this mechanism, which has been termed polarizational recombination in the electron-ion collision literature [3], as the source of the enhanced HHG radiation in heavier noble gases compared to lighter ones. In order to compute the radiation emitted by all electrons to first

approximation, one can compute the acceleration of the active electron in the unscreened Coulomb potential. That is, to compute the acceleration of the recolliding electron as if it recollided with a bare nucleus. The factor of Z, the atomic number, which arises from this descreening, is actually due to the Z-1 bound electrons and one free electron which radiate.

A cartoon illustrating the idea is shown in Fig. J1. Consider an electron that is about to recollide with its parent ion. The electron experiences some force that is exerted on it by the nucleus and the bound electrons. Then if F is the force exerted by a bound electron on the free electron, the

Fig. J1: Illustration of the calculation of the radiation emitted by the bound electrons

total force exerted on the free electron is also F: An attractive force of ZF and a repulsive force of (Z-1)F. The radiation emitted by the free electron is proportional to F, and all Z-1 electrons emit additional radiation proportional to (Z-1)F. The total emitted radiation is therefore proportional to ZF, as if the nucleus were unscreened.

References

[1] M. Lewenstein, P. Balcou, M. Y. Ivanov, A. L'Huillier, and P. B. Corkum, Phys. Rev. A, vol. 49, pp. 2117-2132, 1994.
[2] A. Gordon, F. X. Kärtner, N. Rohringer, and R. Santra, Phys. Rev. Lett., 96, 223902 (2006).
[3] A. V. Korol, F. J. Currell, and G. F. Gribakin, J. Phys. B, vol. 37, pp. 2411-2428, 2004.

K: Broadband Studies of 1-D and 3-D Photonic Crystals

High-index contrast photonic crystal waveguides are of interest for an increasing variety of applications. However, the measurements required to understand the basic physical phenomena of photonic crystal devices often present serious experimental challenges. In many cases it is necessary to perform spectral measurements over 50 – 100% of the center frequency of the device (i.e. as much as an octave) in order to understand the bandgap-related phenomena. Additionally, due to the nano-scale dimensions of such devices, high insertion losses and low throughput are typical in a laboratory setting. It is for this reason that high-brightness sources such as tunable lasers are typically used to scan the broad spectral features of photonic crystals. Unfortunately, tunable laser sources spanning the entire 1 – 2 μm spectral range, critical for the study of telecom-centered devices, are not readily available. To facilitate the science and study of photonic crystals and integrated photonic devices, we develop practical femtosecond fiber-laser-based supercontinuum sources (SC) spanning the 1.2 – 2.0 μm wavelength range and broadband SC based measurement techniques. These techniques are then applied to the study of high index contrast photonic crystal devices, enabling a host of new photonic crystal studies. Experiments involving both 1-D photonic crystal microcavity waveguides and 3-D periodic photonic crystals with embedded point defects are described. Experimental findings are compared with rigorous electromagnetic simulations[1,2].

Earlier applications of SC sources to the study of photonic devices have utilized solid-state Ti:Sapphire-based SC sources (centered at 800 nm) to study two-dimensional photonic crystal slab waveguides with a system utilizing free-space optics [3,4]. While this is an effective means of generating supercontinuum centered at 800 nm, it is difficult to efficiently extend the spectral range past 1.5 microns. Furthermore, the short lengths of photonic crystal fiber used to construct

such sources exhibit severe polarization drift, over time. This can be detrimental to the study of polarization sensitive devices such as photonic crystal waveguides and cavity modes. In contrast, we have developed unpolarized all-fiber SC sources centered at telecommunications wavelengths (1.55 μm) and an all-fiber measurement apparatus for the study of photonic crystals and integrated circuits at telecom wavelengths. To minimize the losses and complexity produced by broadband free-space optics, we focus instead on all-fiber methods for broadband polarization control, and coupling. Additionally, through sensitive detection and careful normalization many of the undesirable aspects of a typical SC source can be mitigated, producing high fidelity measurements over the entire 1.2 – 2.0 μm wavelength range[1,2].

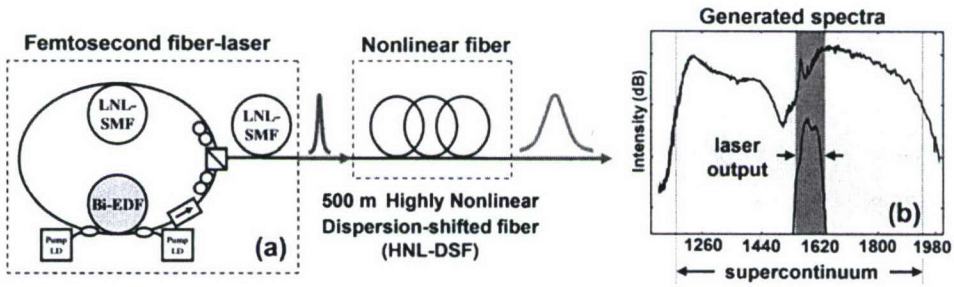

Figure K1: (a) Schematic of supercontinuum source, which consists of a femtosecond fiber-laser and a length of highly nonlinear dispersion shifted fiber. (b) Optical power spectrum of the fiber laser output before and after passing through the nonlinear fiber.

The SC source developed in this work consists of a length of highly nonlinear dispersion-shifted fiber (HNL-DSF) seeded by a femtosecond stretched-pulse fiber laser, shown in Fig. K1(a). The laser consists of a 55.6 cm length of bismuth oxide-based erbium-doped fiber (Bi-EDF), 1.8 m of low-nonlinearity single-mode fiber (LNL-SMF), two polarization controllers, and a polarizing beam-splitter. The rejection port of the polarizing beam splitter forms the output coupler of the laser, while a bi-directionally pumped length of Bi-EDF fiber serves as a the gain medium, providing a broad gain bandwidth and high gain per unit length [5]. To balance the dispersion of the Bi-EDF, and manage the intracavity nonlinearity, 1.8 m of LNL-SMF is included in the laser. Mode-locked operation of the laser was obtained through nonlinear polarization evolution [6]. For pump powers of 350 mW, a 28 mW average output power was obtained with center wavelengths and spectral full-width half maxima of 1571 nm and 58 nm respectively. Through external compression with a 1.8 m segment of LNL-SMF 100 fs pulses were obtained, providing a peak pulse power of ~8.5 kW, which was sufficient for the generation of a broad SC spectrum. Pulses are injected into 500 m of HNL-DSF having a zero-dispersion wavelength of 1565 nm and a nonlinear coefficient of 21 km^{-1} W^{-1} to generate SC. The laser spectra before and after the HNL-DSF are shown in Fig. K1(b). It should be noted that the supercontinuum light generated by this method is unpolarized when measured at millisecond time scales due to nonlinear polarization evolution produced in the HNL-DSF. Additionally, the nonlinear nature of the SC generation makes the shape of the spectral output very sensitive to changes in laser state[7].

The SC spectrum generated in the HNL-DSF is coupled into the apparatus shown in Fig. K2(a) for waveguide transmission studies. The unpolarized SC light is first passed through a broadband fiber-optic coupler, splitting the continuum into two ports, signal and reference. The signal is then sent through an inline polarizer and polarization controller, which define the polarization at the input of the waveguide. A lensed fiber is then used to couple the signal into the waveguide. A second lensed fiber collects the waveguide output that is sent through a polarization controller and inline polarizer for polarization analysis. The signal and reference are then imaged through a monochromator onto two identical photodetectors, for real-time normalization of the SC fluctuations and spectral changes. Detection is performed with Peltier cooled IR-enhanced InGaAs photodiodes and lock-in amplifiers to achieve low noise measurements (with a noise equivalent power of 28 fW/$\sqrt{Hz}$) and enable rapid scans (less than one minute) with as little as 4 mW of SC light.

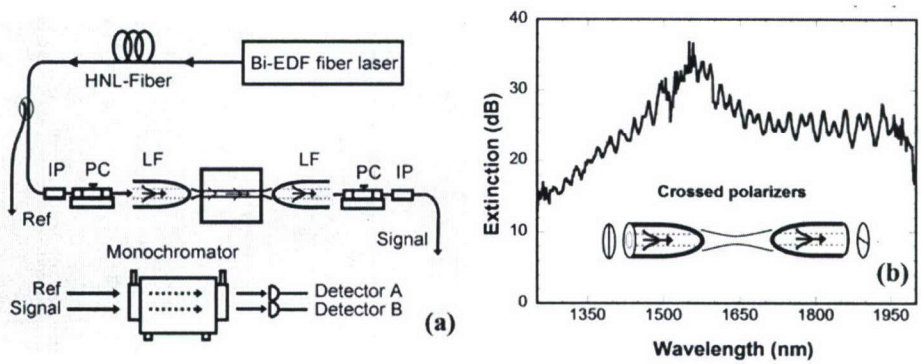

Figure K2: (a) A schematic of measurement apparatus. A small fraction of SC light is diverted by a coupler for reference (Ref) measurement while the remainder (Signal) is passed through the waveguide. The signal and reference are then imaged through a monochromator onto identical photo-detectors for real time normalization. (b) Polarization extinction obtained through polarization control method depicted in Fig 2(a).

Polarization control of the light launched into the waveguide and polarization analysis of the light collected from the guide were performed with use of broadband inline polarizers and strain-type polarization controllers as depicted in Fig K2(a). As seen in Fig. K2(b), this provides greater than 20 dB of polarization extinction over most of the spectral range of the SC source. However, critical to broadband performance is (1) the type of inline polarizer used, and (2) minimization of polarization mode dispersion (PMD) which follows the polarizer. Laminated inline polarizers of the type described in ref [8] were used, providing high extinction and low insertion losses over the entire 1 – 2 μm wavelength range. PMD was managed by minimizing the length of fiber between the polarizer and lensed fiber, as well as any bending experienced by the fiber. For the measurement shown in Fig K2(b), fiber lengths were kept below 30 cm. Additionally, through a slight change in the state of the polarization controller >25 dB contrast can be achieved at any wavelength in the 1.2 – 2.0 μm range, enabling higher polarization extinction through more than one wavelength scan if needed.

This method was applied to the study of a number of HIC devices. For this report we examine a 1-D photonic bandgap microcavity and 3-D photonic crystal with point defects [2]. The 1-D photonic crystal microcavity, which has been studied extensively over the past several years, consists of a silicon strip on top of an oxide layer, forming a waveguide with a single TE-like mode over much of the 1 – 2 μm wavelength range [9,10]. A photonic crystal is patterned in the waveguide by etching a periodic array of holes through the silicon strip. The photonic crystal defect is then defined by increasing one hole spacing from a (the lattice constant) to a_d (the defect length). A device schematic and scanning electron micrograph (SEM) are shown in Fig. 3(b). For comparison with experiments, simulations of the device band structure and power transmission were performed based on the parameters extracted from SEM measurements [11,12]. Results of the band-structure computations can be seen in Fig K3(a) while the dashed curve of Fig K3(c) shows the simulated power transmission.

Superposed on the photonic-crystal theoretical power transmission curve (dash) of Fig. K3(c) is the measured transmission spectrum (solid). The experimental spectrum was obtained by measuring the photonic crystal waveguide transmission and normalizing to a calibration scan of an identical waveguide without a photonic crystal. Normalization is important to remove wavelength dependence of waveguide coupling, waveguide propagation losses as well as spectral variations of the SC source. However, a comparison of theory with experiment reveals that normalization is quite effective. Remarkable agreement is seen between experiment and theory for wavelengths between 1400 – 2000 nm. A 265 nm stop-band is clearly visible in the experiment from approximately 1425 – 1690 nm. In addition, the high resolution spectrum shown in Fig. K3(d) reveals a sharp microcavity resonance can be seen at 1542 nm, demonstrating

efficient power coupling through the photonic crystal, with approximately 52% transmission. This is in reasonable agreement with the simulated transmission efficiency of 68%.

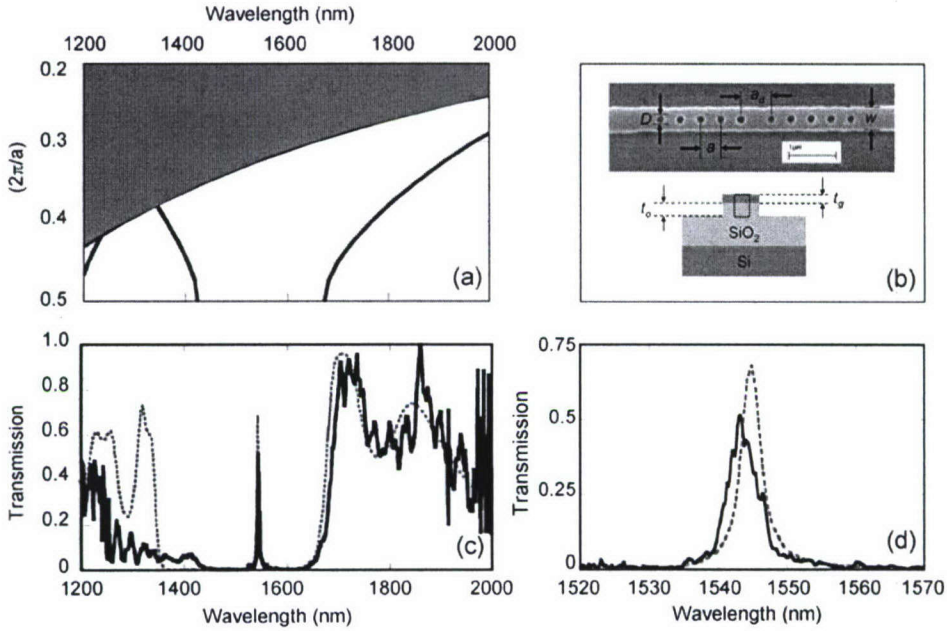

Figure K3: (a) Band diagram (TE-like bands only) based on SEM measurements of device. Grey region indicates states above the light line. (b) SEM of microcavity (top) and cross-section of waveguide (bottom). Device parameters extracted from SEM are a = 424 nm, a_d = 649 nm, w = 494 nm, t_g = 195 nm, t_o = 350 nm, and D = 179 nm. (c) A transmission measurement (solid) and simulated transmission (dashed) of photonic crystal microcavity (TE polarization). The transmission measurement is normalized to that of a similar waveguide without etched holes. (d) High resolution (0.1 nm) measurement (solid) and simulation (dashed) of the microcavity resonance.

A similar supercontinuum based technique was applied to the study of a 3D photonic crystal with embedded point defects, enabling high spatial resolution studies (with a 2.5 μm spot size) of a small number of embedded point defects which were randomly distributed within the PhC. An SEM of the 3-D PhC under study can be seen in Fig. K4(c), and was fabricated in Silicon through a layer-by layer process utilizing several successive e-beam lithography steps. This 3-D photonic crystal exhibits a 21% complete photonic bandgap centered at telecom wavelengths. The details of this fabrication process can be found in reference [1]. The fabricated structure consists of alternating layers of two complementary 2-D photonic crystal slabs, one layer of dielectric rods and another of air holes in a dielectric slab. Embedded within the PhC are randomly distributed defects, each consisting of a completely filled air hole. Defects of this type produce a spatially localized photonic crystal mode, having numerous resonant states within the photonic bandgap, which couple to radiation. These defects are dispersed within the photonic crystal with a density of 15%. Despite the remarkable fabrication quality, inhomogeneity in the local environment of these point defects was unavoidable and resulted in inhomogeneous broadening of defect states throughout the PhC. For this reason it was necessary to probe very small areas of the PhC to resolve the energy spectrum of individual defect cavities. Spectroscopic studies of these defects over small areas proved difficult with thermal white light sources due to their low brightness. However, SC based measurement techniques yielded high fidelity measurements of a small number of nano-scale PhC defects, allowing the energy spectrum of individual defects to be fully resolved.

In this study, supercontinuum-based confocal reflection and transmission measurements were used to examine a small number of defects embedded within the PhC. An average of 3 PhC defects could be studied with use of a Gaussian spot size of 2.5 μm generated by a lensed fiber. The supercontinuum source used in these studies consisted of a Ti:Sapphire-pumped optical

parametric oscillator (OPO) which was used to seed the SC generation in a highly nonlinear fiber, generating SC spanning 1.2 – 2.0 μm. Further details about the SC source are described in *Rakich et. al.* [13]. In these experiments, a reference channel was used to normalize for any spectral variations; however, unpolarized SC light was sufficient to observe the defect resonances, making polarization control unnecessary.

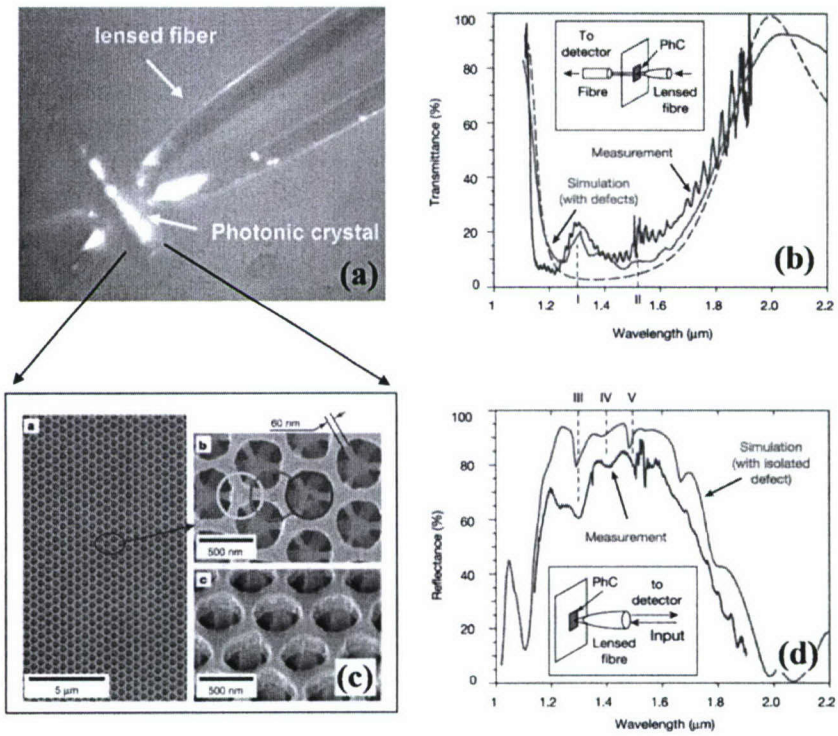

Figure K4: (a) photo of lensed fiber and photonic crystal 3D PhC device under test (b) Theoretical (aqua) and experimental (red) transmission spectra of 3D PhC with defects. Theoretical transmission of PhC without defect states (green dash). (c) SEM of 3D fabricated SEBL (d) Theoretical (aqua) and experimental (red) reflection spectra of 3D PhC with point defects.

Spatially localized reflection measurements, taken by this method, were performed at numerous positions on the photonic crystal. Some characteristic reflection and transmission measurements can be seen in Figs. K4(b) and (d) along with the corresponding theoretical transmission and reflection spectra computed through 3D FDTD computations. The experimental geometry for the transmission measurement is depicted in the inset of Fig. K4(a). Here a lensed fiber forms a 2.5 μm Gaussian spot size on the PhC, while a flat-cleaved single mode fiber optic was used to collect the light transmitted through the PhC over a narrow range of transverse wave-vectors (corresponding to ~1° half angle). The PhC transmission spectrum was then normalized to a similar measurement through the same substrate, without the PhC in the path. We can see that the bandgap of the PhC is clearly resolved along with two peaks in the transmission spectrum (denoted by I & II in Fig. K4(b)), corresponding to resonant transmission through the multi-mode point defects. This can be seen by comparing the theoretical (aqua) and experimental (red) transmission spectra. Such peaks in transmission are not found in simulations of the structure without defect states (green), clearly indicating that these spectral features result from resonant transfer of power through the defect modes. The spectral signatures of the defect modes are somewhat less pronounced for the transmission spectrum, however, more striking features resulting from the defect states are observed as dips in the reflection spectrum. This is because the reflection measurement probes a large transverse wave-vector range (corresponding to a 15.5° half angle), which is more suitable for coupling to localized defect states which tend to

radiate over large solid angles. A detailed comparison of the experimental (red) and theoretical (aqua) reflection spectra can be made from Fig K4(d). Three dips are observable in the reflection spectrum at approximately 1.4 μm, 1.5 μm and 1.6 μm wavelengths (denoted by III, IV & V in Fig. K4(d)), which result from resonant coupling to localized defect states within the PhC. The observed stop band and the positions of the defect resonances are in remarkable agreement with the simulated reflection spectrum. It should also be noted that all parameters used to simulate the transmission spectra shown below were extracted from SEMs of the device, and no free parameters were used.

References

1 Qi, M. H. et al. A three-dimensional optical photonic crystal with designed point defects. *Nature* 429, 538-542 (2004).
2. Rakich, P. T. et al. Nano-scale photonic crystal microcavity characterization with an all-fiber based 1.2-2.0 mu m supercontinuum. *Opt. Express* 13, 821-825 (2005).
3. Neal, R. T. et al. Ultrabroadband transmission measurements on waveguides of silicon-rich silicon dioxide. *Appl. Phys. Lett.* 83, 4598-4600 (2003).
4. Netti, M. C. et al. Separation of photonic crystal waveguides modes using femtosecond time-of-flight. *Appl. Phys. Lett.* 81, 3927-3929 (2002).
5. Kuroiwa, Y. et al. in *OFC 2001. Optical Fiber Communication Conference and Exhibition. Technical Digest, 17-22 March 2001* 5-1 (Opt. Soc. America, Anaheim, CA, USA, 2001).
6. Haus, H. A., Tamura, K., Nelson, L. E. & Ippen, E. P. Stretched-Pulse Additive-Pulse Mode-Locking in Fiber Ring Lasers - Theory and Experiment. *IEEE J. Quantum Electron.* 31, 591-598 (1995).
7. Newbury, N. R., Washburn, B. R., Corwin, K. L. & Windeler, R. S. Noise amplification during supercontinuum generation in microstructure fiber. *Opt. Lett.* 28, 944-946 (2003).
8. Shiraishi, K., Hatakeyama, H., Matsumoto, H. & Matsumura, K. Laminated polarizers exhibiting high performance over a wide range of wavelength. *J. Lightwave Technol.* 15, 1042-1050 (1997).
9. Foresi, J. S. et al. Photonic-bandgap microcavities in optical waveguides. *Nature* 390, 143-145 (1997).
10. Wong, C. W. et al. Strain-tunable silicon photonic band gap microcavities in optical waveguides. *Appl. Phys. Lett.* 84, 1242-1244 (2004).
11. Johnson, S. G. & Joannopoulos, J. D. Block-iterative frequency-domain methods for Maxwell's equations in a planewave basis. *Opt. Express* 8, 173-190 (2001).
12. Kunz, K. S. & Luebbers, R. J. The finite-difference time-domain method for electromagnetics. (CRC Press: Boca Raton, 1993).
13. Rakich, P. T. et al. in *2004 IEEE LEOS Annual Meeting Conference Proceedings, LEOS 2004, Nov 7-11 2004* 813-814 (Institute of Electrical and Electronics Engineers Inc., Piscataway, NJ 08855-1331, United States, Rio Grande, Puerto Rico, 2004).
14. Rakich, P. T. et al. Invited Paper, *in 2005 NOC Proceedings for European Conference on Networks and Optical Communications, July 5-7 2005 p 4-11* (University College London, London, UK)
15. Rakich, P. T. et. al. Invited Paper, *Optics East Annual Meeting Conference Proceeding, Oct. 25-28 2005* (Copley Marriot, Boston MA, USA)

L: Ultra-wide Tuning of Photonic Microcavities via Evanescent Field Perturbation

The field of integrated optics promises to provide a practical and scaleable means of routing and switching light for applications ranging from telecommunications networks to sensing and spectroscopy. However, a key barrier to the development of dynamic integrated optical circuits is the lack of a practical means of enabling large changes in waveguide *effective-index* (Δn_{eff}). Large Δn_{eff} is critical for the development of widely tunable filters and for scaling active components to smaller size. Currently, thermo-optic tuning is the only widely implemented

means of producing a Δn_{eff} in optical circuits [1-3], but it has insufficient range and is slower than desired for many applications.

We have demonstrated ultra-wide tunability through evanescent perturbation of a large free-spectral-range (FSR) micro-ring resonator. Geometrical tuning mechanisms, such as evanescent tuning, have the distinct advantages that they are material-system independent and that they enable large Δn_{eff} with small power dissipation. In what follows, a 1.7 % frequency shift is demonstrated (or 27 nm tuning near 1565 nm) in a microring resonator without significant distortion of the cavity resonance. Furthermore, complete recovery of the resonance is found when the perturbing body is removed. Experiments are carried out with a novel silica-fiber probe which provides access to the evanescent field of an air-clad high-index-contrast (HIC) ring-resonator mode. As the probe is advanced toward the ring resonator, the probe-ring distance is found through simultaneous nanometric distance calibration and force measurements.

For the purposes of this study, a silicon-rich silicon-nitride ring resonator of the type described in Ref. 4, but of first order, is considered. The ring resonator was designed for operation at 1.5 μm wavelengths, with an FSR of 27 nm. The mode of the air-clad ring resonator has an evanescent field extending outside the guide in the direction normal to the plane of the ring. Consequently, a dielectric body can be placed above the ring such that it uniformly penetrates the evanescent field of the ring (see inset of Fig. L1(b)). This produces an increase in effective index of the mode, resulting in a shift of resonance frequency. If the perturbing dielectric is comprised of silica, a maximum theoretical tuning range of 29.9 nm at an operating wavelength of 1565 nm is possible. The tuning closely approximates an exponential as a function of distance z from the ring, with a decay length of $1/\alpha \cong 91.6$ nm, making it evident that a high degree of positional control is required.

The major challenge in a laboratory implementation of the geometry shown in Fig. L1(b) is the high degree of angular alignment required between the perturbing body and the ring resonator (typically microradians). This alignment issue is addressed through a novel probe design illustrated in Fig. L1(a). It utilizes a fiber-taper near the end of the probe, which allows the fiber end to lie parallel to the surface when in contact with the substrate of the ring resonator. The fabrication process for this probe is outlined in the inset of Fig. L1(a). First, the fiber is tapered to several microns, forming a flexible joint. Then the face of the probe (used to perturb the ring resonator) is formed by a fiber cleave, and annealed until a small amount of glass reflow occurs, ensuring an ultra-smooth surface.

The apparatus used to perform evanescent perturbation experiments can be seen in Fig. L1(a). It consists of the silica fiber probe (described above), which is mounted on a cantilever having a force constant of ~5000 N/m. The probe-cantilever assembly is advanced with a distance-calibrated piezo translation stage such that it can be brought in and out of contact with the ring-resonator device. Motion of the cantilever and probe relative to the device is monitored with an interferometer, one end of which is formed by the cantilever. Position is read through rapid interrogation of the interferometer with white light from an erbium-doped fiber amplifier (EDFA) and an optical spectrum analyzer (OSA). Force experienced by the probe can be precisely measured from the cantilever deflection. Broadband EDFA light is also coupled into and collected from the ring resonator device with lensed fibers to measure the micro-ring response. Experiments were performed by simultaneously measuring the ring resonator drop response, cantilever position, and forces of probe-sample interaction.

The results of a tuning experiment can be seen in Figs. L1(c)-(e). Fig. L1(c) shows the ring resonance frequency as a function of the cantilever height measured by the interferometer. Each data point (circle) represents the resonant wavelength obtained from measurements of the drop port of the ring resonator. The force and force derivative experienced by the probe over the same range of cantilever displacement are displayed in Fig. L1(d-e). In Fig. L1(d) two trends can be seen: (1) for smaller positions (i.e. position $\leq$ 1270 nm) an exponential change in resonance wavelength covers a 25 nm tuning range; (2) for positions larger than 1270 nm (indicated by the

vertical dashed line) there is a very gradual change in ring resonance frequency. In interpreting these two tuning regimes, the forces of interaction between the probe and sample (seen in Fig. L1(b)) provide insight. For the evanescent tuning regime attractive forces (negative in sign) are experienced by the probe, which are due to a combination of capillary and Van der Waals interactions as the probe approaches flush contact [5]. Snap-down of the probe can be seen at 1270 nm most clearly through a sharp increase in the derivative of the force, corresponding to the maximum in the exponential portion of the tuning curve. After this point, the probe remains flush with the device resulting in compression of the probe, which is seen as a large positive slope in the force curve.

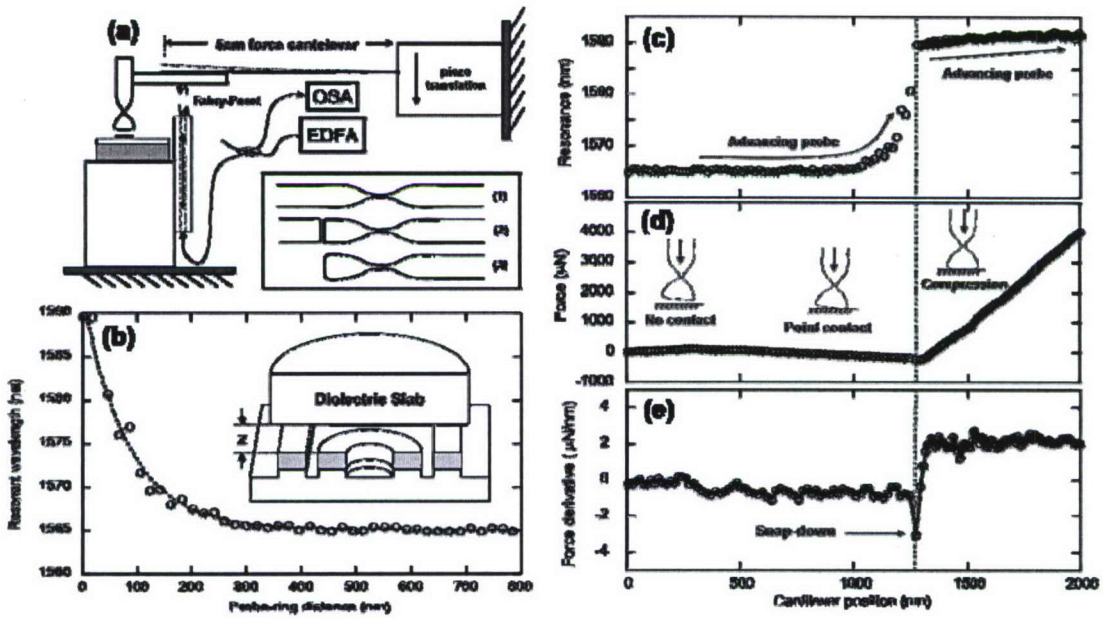

Fig. L1. (a) Tuning apparatus and (inset) probe fabrication process; (b) measured resonance wavelength of microring vs. distance of probe from ring surface (inset – schematic of tuning geometry); (c,d,e) resonance wavelength, force and force derivative vs. cantilever position.

Through an analysis of the force and force derivative measurements, the probe-ring distance can be placed on an absolute scale and compared with theory, as seen in Fig. L1(b). An exponential fit of the tuning versus probe-ring distance reveals a decay length of 87 ± 4 nm and a maximum tuning of 24.8 nm, which agrees with the theoretical decay length of 91.6 nm and maximum tuning range of 29.9 nm. Tunings as large as 27 nm were obtainable by contacting the ring using unique points of the probe face, indicating that conformation of the probe surface plays a role in limiting the maximum possible perturbation. High-speed acquisition of spectra shows that throughout the tuning process the resonance shape appears to be preserved. Additionally, when the fiber is raised again the unperturbed resonance is fully recovered, demonstrating a negligible degree of hysteresis, which suggests no material exchange between the probe and ring.

High-fidelity reversible tuning was demonstrated over 1.7% frequency range through evanescent tuning. In this experiment, a uniform silica perturbing body was used, although it should be noted that with higher-index perturbing structures, upwards of 3% tuning could be implemented through the same range of motion. Furthermore, higher index-contrast waveguides (such as silicon) can tolerate stronger perturbation before coupling to radiation modes occurs, which should further enhance tuning ranges. For more information see Ref [6].

References

1. P. Heimala, P. Katila, J. Aarnio and A. Heinamaki, "Thermally tunable integrated optical ring resonator with poly-Si thermistor," J. Lightwave Tech. 14, 2260-7 (1996).

2. D. Geuzebroek, E. Klein, H. Kelderman, N. Baker and A. Driessen, "Compact wavelength-selective switch for gigabit filtering in access networks," IEEE Photon. Tech. Lett. 17, 336-8 (2005).
3. H. M. H. Chong and R. M. De La Rue, "Tuning of photonic crystal waveguide microcavity by thermooptic effect," IEEE Photon. Tech. Lett. 16, 1528-1530 (2004).
4. T. Barwicz et al. "Microring-resonator-based add-drop filters in SiN: fabrication and analysis," Opt. Express 12, 1437-1442 (2004).
5. W.M. van Spengen, R. Puers and I. de Wolf, "A physical model to predict stiction in MEMS," J. Micromech. and Microeng. 12, 702 (2002).
6. Rakich, P.T., et al., "Ultrawide tuning of photonic microcavities via evanescent field perturbation," Opt. Lett., 31,1241-3 (2006)

M: Propagation Without Diffraction in a 2-D Photonic Crystal

One of the interesting effects observed in photonic crystals (PhCs) is the propagation of optical beams without diffraction. Referred to as super-collimation (or self-collimation), this optical effect allows diffraction-free propagation of micron-sized beams over centimeter-scale distances. It is a natural result of the unique dispersive properties of PhCs, and no nonlinearities or physical waveguides are required. Self-collimation was first observed by Kosaka et al. in a 3D PhC [1] and by Wu et al. in 2D triangular [2] and square [3] lattices, over relatively short distances (hundreds of microns). We have recently reported centimeter-scale super-collimation in a large-area 2D photonic crystal [4]. A natural metric for the scale of collimation experiments is the isotropic diffraction-length over which a Gaussian optical beam would normally spread by a factor of $2^{1/2}$ in an isotropic medium: $L_d = \pi.\omega^2 / \lambda_x$ where ω is the Gaussian beam waist radius and $\lambda_x = 2\pi / k_x$ is the wavelength of the light in the direction of propagation. A figure of merit for super-collimation is the ratio of the observed length of collimated propagation to the isotropic diffraction length L_d. The utility of super-collimation is strongly linked to the distance over which it can be maintained, and the figure of merit is important since it dictates the maximum density and complexity of optical circuits based on super-collimation. Previous experimental studies showed figures of merit smaller than 6 [5]. In this work we observe figures of merit of more than 600.

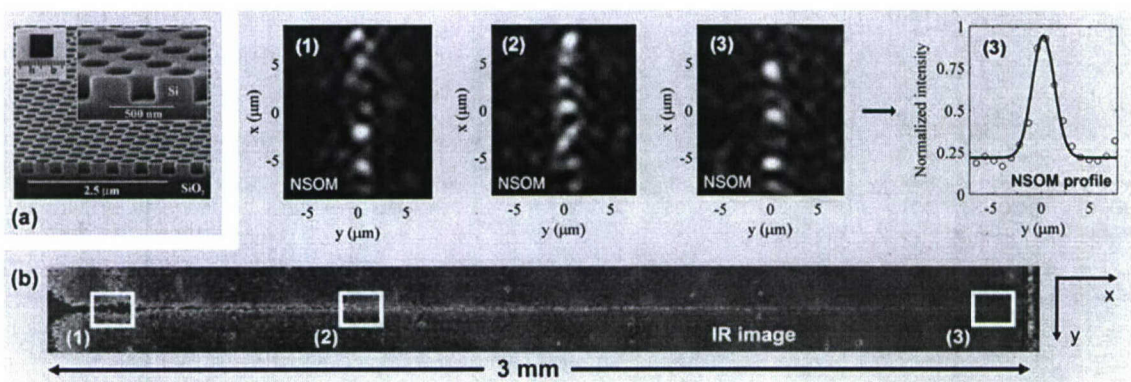

Figure M. Super-collimation over a 0.3 cm sample. **(a)** SEM image of the fabricated large-area PhC. **(b)** Top view of the TE-light guided along a 0.3 cm-long PhC, acquired with an IR camera, and NSOM images of the collimated beam at positions labeled (1)-(3) (corresponding to 0.02, 0.10 and 0.30 cm along the device), and beam cross-section with Gaussian fit, obtained from the intensity map at position (3).

Super-collimation is studied over centimeter-length-scale distances in a large-area 2D PhC with a square lattice of air holes in a thin silicon film – Figure M1(a). Our 2D PhC was fabricated in a silicon on insulator (SOI) wafer, using interferometric lithography and reactive ion etching [6], and was designed to operate in the 1500 nm wavelength range for TE radiation (electric field parallel to the 2D plane), in the lowest energy band (close to the edge of the bandgap). The lattice

constant is a = 350 nm and the hole radius is r = 0.3a. The projected band structure of the PhC slab under study was computed with a 3D frequency-domain eigenmode solver, and around λ = 1500 nm the computed surfaces showed remarkably little spatial dispersion in the transverse wavevector.

We observed experimentally that the optimum wavelength for super-collimation was approximately 1500 nm, and we measured losses of (3.6 ± 0.5) dB/mm. A coarse contact-mode near field scanning optical microscopy (NSOM) technique [7] was used to obtain high resolution images of the beam profile at different positions along the PhC, showing that a 2 μm-wide beam was conserved over 0.3 cm of propagation – Figure M1(b). The beam profiles were fitted to Gaussian functions yielding full widths at half maximum (FWHMs) in intensity of 2.1, 2.1 and 2.3 (±0.2) μm, for positions (1)-(3), respectively. In addition, high-resolution confocal measurements confirmed super-collimation after 0.5 cm of propagation – Figure M2.

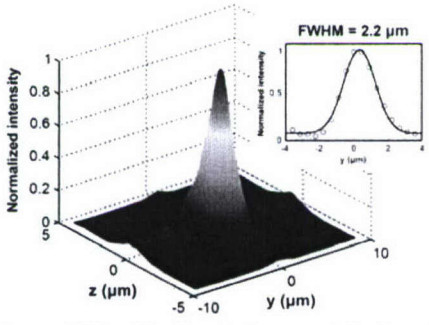

Figure M2. Confocal image (displayed as a surface-plot) at the output of a 0.5 cm-long PhC, showing the TE beam profile at the super-collimation wavelength. The inset shows a Gaussian fit to the data and returns a FWHM of 2.2 μm.

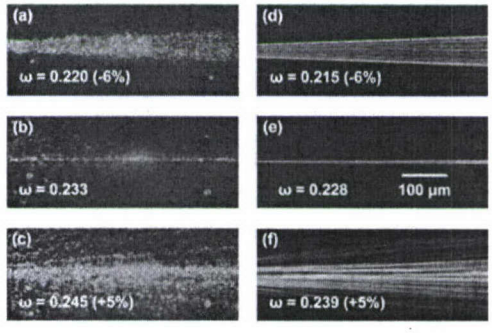

Figure M3. Frequency dependence and disorder effects on super-collimation. (a-c) Experimental results. (d-f) Simulated results through BPM.

The results of this experiment show figures of merit as high as 376, which correspond to super-collimation over more than 14,200 lattice constants. Additional studies of a 0.8 cm-long PhC device yielded measurements of beams with similar transverse profiles, and figures of merit closer to 600. Both frequency dependence and effects of disorder were observed experimentally – Figure M3(a-c) – and studied through the beam propagation method (BPM), based on the computed dispersion surfaces – Figure M3(d-f). For a normalized frequency of $\omega = a/\lambda = 0.233$ the beam divergence is negligible. The discrepancy between measurements and simulations is 2%, and the beam break up is due to short scale disorder, such as fabrication roughness (RMS fluctuation in the hole-radius of 0.6 nm). We show that super-collimation possesses inherent robustness with respect to short-scale disorder and this work presents an important step toward enabling flexible high density optical interconnects.

References

1 H. Kosaka, T. Kawashima, A. Tomita, M. Notomi, T. Tamamura, T. Sato, and S. Kawakami, "Self-collimating phenomena in photonic crystals," Appl. Phys. Lett. 74, 1212-1214 (1999).

2 L. J. Wu, M. Mazilu, and T. F. Krauss, "Beam steering in planar-photonic crystals: from superprism to supercollimator," J. Lightwave Technol. 21, 561-566 (2003).

3 L. Wu, M. Mazilu, J.-F. Gallet, and T. F. Krauss, "Square lattice photonic-crystal collimator," Photonics and Nanostructures - Fundamentals and Applications 1, 31-36 (2003).

4 P. T. Rakich, M. S. Dahlem, S. N. Tandon, M. Ibanescu, M. Soljačić, G. S. Petrich,, J. D. Joannopoulos, L. A. Kolodziejski, and E. P. Ippen, "Achieving centimetre-scale supercollimation in a large-area two-dimensional photonic crystal," Nature Mater. 5, 93-96 (2006).

5 H. Kosaka, T. Kawashima, A. Tomita, T. Sato, and S. Kawakami, "Photonic-crystal spot-size converter," Appl. Phys. Lett. 76, 268-270 (2000).
6 S. N. Tandon, M. Soljačić, G. S. Petrich, J. D. Joannopoulos, and L. A. Kolodziejski, "The superprism effect using large area 2D-periodic photonic crystal slabs," Photon. and Nanostruct. 3, 10-18 (2005).
7 S. Bourzeix, J. M. Moison, F. Mignard, F. Barthe, A. C. Boccara, C. Licoppe, B. Mersali, M. Allovon, and A. Bruno, "Near-field optical imaging of light propagation in semiconductor waveguide structures," Appl. Phys. Lett. 73, 1035-1037 (1998).

N: Laser Micro-Machining of Photonic Devices

Micromachining using femtosecond laser pulses is a powerful and versatile technique for fabricating photonic devices. It is capable of writing three-dimensional structures and has the potential for high-density integrated photonic circuits, thus providing enhanced functionality not possible in planar geometries. In contrast to the conventional semiconductor-based fabrication process, the micromachining process utilizes relatively simple equipments, allowing for rapid construction of a variety of devices. Important elements of the fabrication system consist of a femtosecond laser and computer controlled three-dimensional stages.

Specifically, we are using a three-axis air-bearing stage system that provides nanometer resolution and full three-dimensional computer control. Typically glass samples are located on top of the stages and moved according to software commands, while femtosecond pulses are focused inside the samples. In our case, those pulses are emitted from a homemade extended cavity Kerr-lens-modelocking Ti:Sapphire laser with ~150-nJ energy. The repetition rate and pulse duration of the oscillator are 5.85 MHz and 45 fs, respectively [1]. In contrast to amplified lasers, it has the repetition rate high enough to accumulate heating effects, which enables device fabrication approximately three orders of magnitude faster than the amplified laser case. Moreover, generally MHz-range lasers are advantageous for fabricating waveguide devices since the photomodification is caused mainly by thermal diffusion, resulting in symmetric cross-sections of modified regions, while kHz amplified lasers cause elliptical cross-sections due to nonlinear absorption and plasma generation highly dependent on the focal volume [2]. Finally, the relative high energy in our laser system enables us to overcome the restriction to very high numerical aperture objectives, thus giving greater flexibility and versatility to the machining process.

Since the first demonstration for modifying refractive indices in glass materials [3], various structures have been fabricated via direct writing using femtosecond lasers [4-17]. They include not only a wide variety of planar devices, such as several types of couplers [4-7], interferometers [8, 9], and active waveguides [10, 11] but also three-dimensional structures, such as optical splitters [12, 13], interconnections [14], wavelength-division multiplexing couplers [15], and directional couplers [16, 17]. In following sections, we will discuss the telecom-wavelength characterization of waveguides and measurement results of 3x3 couplers we recently fabricated.

Basic Characterization of Waveguides

After photonic devices are directly written in a glass substrate, usually its surfaces where the beam is coupled are polished for efficient light coupling. Then, it is located on a waveguide manipulator sandwiched between two XYZ stages holding fibers. Either amplified spontaneous emission (ASE) from an Erbium-doped fiber amplifier (EDFA) or the light emitted from a 1.5μm tunable laser source is coupled into waveguides written in the substrate. Another butt coupled fiber at the other side of the substrate picks up waveguide outputs, enabling readings from an optical spectrum analyzer or power meter. To minimize coupling losses, index matching oil is applied between the fiber tips and waveguide surfaces. A charge-coupled device (CCD) camera with a microscope objective is used for alignment.

To analyze basic properties of direct written waveguides, we fabricated the structure shown in Fig. N1(a), consisting of straight and curved waveguides, in soda lime glass substrates (Corning 0215, n=1.515), while varying the parameters, such as laser power, beam polarization, bending radius, and writing speed. When the writing speed was too fast and the writing power was too low, we observed weaker confinement of light, leading to larger output beam profiles. On the other hand, when the exposure is too high, i.e., in the case of high power and low speed, multimode guiding occurs. Typically, nicely guided single-mode beam profiles, as shown in Fig. N1(b), were observed when the pulse energy is approximately ~15 nJ and the writing speed ranges from 5 mm/s to 20 mm/s.

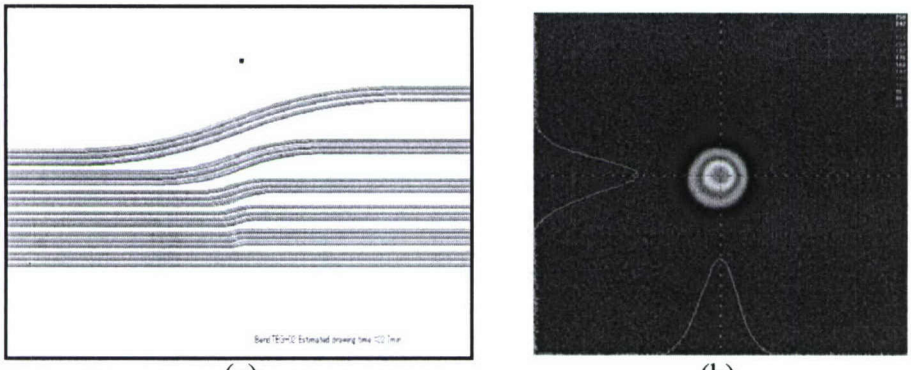

(a) (b)

Figure N1. (a) Layout of the structure for measuring basic properties of direct written waveguides. (b) Typical near-field beam profile at the waveguideexit

One important property of a waveguide is its loss. We measured losses of straight and curved waveguides for different parameters. In the straight waveguide case (bottom part in Fig. N1(a)), while varying the beam polarization and writing speed, we measured insertion losses for different lengths of waveguides to find out propagation and coupling losses. Fig. N2(a) shows the losses as functions of writing speed when the pulse energy was ~18 nJ. For both polarizations, the propagation loss was the lowest with the speed of 10-20 mm/s and the coupling loss got slightly lower when the speed decreased. Typical propagation and coupling losses were approximately

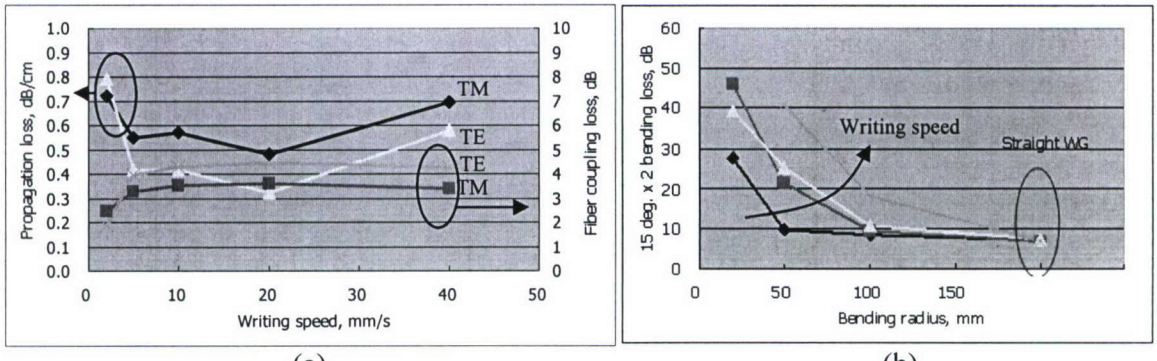

(a) (b)

Figure N2. Losses as functions of writing speed (a) for straight waveguides with transverse-magnetic (TM) and transverse-electric (TE) polarized fields and (b) for S-bends with speeds of 2, 5, 10, and 20 mm/s

0.4 dB/cm and 4 dB, respectively. In the curved waveguide case, we fabricated the S-type bend consisting of two arcs with identical bending angles of 15 degrees but radii of curvatures opposite in sign, as shown in Fig. N1(a). We used radii of 5, 10, 20, 50, and 100 mm. When the insertion loss is measured for the waveguide, it will include transition losses between straight and curved parts and between the arcs. However, the loss caused by radiation along the curved parts dominates. Fig. N2(b) shows the insertion loss as a function of bending radius, as measured for different writing speeds. As well known, the bending loss increases as the radius gets smaller.

Also, the plot shows that as the writing speed decreases, the bending loss gets lower, indicating that the curves with higher refractive-index cores have reduced radiation.

3x3 Couplers

One of the important applications of optical, symmetric 3x3 directional couplers [18] is optical interferometer-based sensors because they enable the detection of the direction of an interferometer arm phase change caused by an analyte. A Michelson interferometer-based low-coherence reflectometer and optical coherence tomography have already been demonstrated via symmetric 3x3 couplers for optical signal processing [19, 20]. Although those couplers were based on fiber optics, the integrated optical type is preferable because it offers such advantages as flexibility in photonic circuit configuration and mass production. Even in an integrated optic form, it is important to maintain the symmetry of the waveguide arrangement in the coupling region in order to be able to detect the direction of phase change efficiently in Mach-Zehnder interferometer-based sensors. In contrast to conventional waveguide fabrication techniques utilizing photolithography and dry etching, direct writing via femtosecond lasers is suitable for realizing three-dimensional devices such as symmetric 3x3 directional couplers.

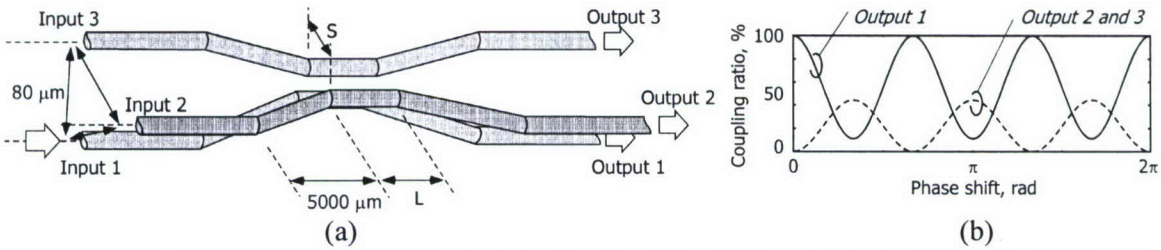

Figure N3. (a) Schematic configuration of a 3x3 directional coupler, and (b) Typical coupling characteristics of an optical, symmetric 3x3 directional coupler.

We demonstrated and characterized symmetric 3x3 three-dimensional directional couplers. Fig. N3 shows the schematic configuration of a symmetric 3x3 coupler and its typical coupling characteristics. The coupler consists of three input waveguides, a transition region, a coupling region, a second transition region, and output waveguides. Fig. N3(b) shows the calculated coupling characteristics of an ideal symmetric coupler, where an optical signal is launched into input port waveguide 1. It should be noted that the optical power of waveguide 1 gradually couples with waveguides 2 and 3 at the same ratio, but it never falls to zero. This is because part of the input optical signal, which couples with waveguide 2, is transferred back to waveguides 3 and 1. The same is true of the part of the input signal that couples with waveguide 3, and is transferred back to waveguides 2 and 1. In other words, if we launch an optical signal from input port 1 and monitor output 1, then the coupler becomes an asymmetric directional coupler. Therefore, output 1 does not fall to zero.

The center-to-center separations between the input and output waveguides were fixed at 80 μm, while the separation in the coupling region was varied between 15, 20, and 25 μm in order to investigate the coupling characteristics. The horizontal length of the transition waveguide regions was fixed at 5 mm. Therefore, the junction angles between the transition waveguide regions and the input and the output, and the coupling waveguide region, varied from 0.43 to 0.36 degrees, according to the waveguide separation and the length of the coupling region. This variation in angle has a negligible effect on the coupling characteristics. Fig. N4 shows the coupling characteristics of the various 3x3 directional couplers at a wavelength of 1530 nm. The solid and dotted lines represent the coupling characteristics for TM and TE polarized modes, respectively. Only a small polarization dependence of 11 % in the coupling ratio is observed in the coupler with a separation of 25 μm and a coupling interaction length of 7.2 mm. This fact supports the idea that a waveguide fabricated with a high-repetition-rate ultra short pulse laser does not show polarization dependence [21]. The measured losses were 6.6 dB and varied only by 0.2 dB as the

separation distance was varied from 25 μm to 15 μm. The excess loss includes propagation loss as well as fiber coupling loss. The small loss variation of 0.2 dB with waveguide separation distance was caused by the discontinuities between waveguides, implying that the effect of the nonadiabatic connection along transition waveguide was negligible. As shown in Fig. N4, the separation S between the waveguides in the coupling region clearly affected the coupling characteristics. Fig. N4(a) illustrates that almost no coupling occurred for a coupling length of 0 μm for a separation of 25 μm. On the other hand, with separations of 20 and 15 μm, a nonzero amount of power has already been transferred when the straight waveguide interaction length is 0 μm, as shown in figures N4(b) and (c). This is because the coupling between the waveguides in the transition region becomes dominant. In either case, the measured coupling characteristics oscillated as a function of the straight waveguide interaction length. This indicates that, despite some errors, it is possible to realize coupled mode functions that are sinusoidal. However, it should be noted that the optical power of waveguide 1 falls to zero for interaction lengths of 7000, 3000, and 800 μm for separations of 25, 20, and 15 μm, respectively. Through numerical calculation, we found that this error resulted from deviations from symmetry dominated by vertical position errors of the coupling waveguide.

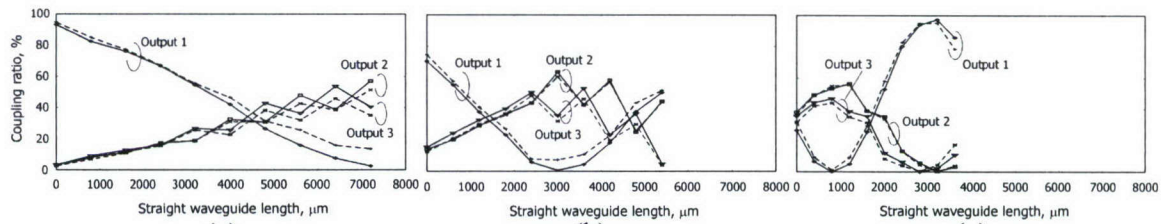

Figure N4. Coupling characteristics of a fabricated 3x3 directional coupler with an optical signal incident from input port 1. The separation S were designed to be (a) 25 μm, (b) 20 μm, and (c) 15 μm. The solid lines and dotted lines correspond to TM and TE polarization modes, respectively.

References

[1] A. M. Kowalevicz, A. T. Zare, F. X. Kartner, J. G. Fujimoto, S. Dewald, U. Morgner, V. Scheuer, and G. Angelow, "Generation of 150-nJ pulses from a multiple-pass cavity Kerr-lens mode-locked Ti : Al2O3 oscillator," *Optics Letters* 28(17): 1597-99 (2003).

[2] S. M. Eaton, H. B. Zhang, and P. R. Herman, "Heat accumulation effects in femtosecond laser-written waveguides with variable repetition rate," *Optics Express* 13(12): 4708-16 (2005).

[3] K. M. Davis, K. Miura, N. Sugimoto, and K. Hirao, "Writing waveguides in glass with a femtosecond laser," *Optics Letters* 21(21): 1729-31 (1996).

[4] D. Homoelle, S. Wielandy, A. L. Gaeta, N. F. Borrelli, and C. Smith, "Infrared photosensitivity in silica glasses exposed to femtosecond laser pulses," *Optics Letters* 24(18): 1311-13 (1999).

[5] C. B. Schaffer, A. Brodeur, J. F. Garcia, and E. Mazur, "Micromachining bulk glass by use of femtosecond laser pulses with nanojoule energy," *Optics Letters* 26(2): 93-5 (2001).

[6] A. M. Streltsov and N. F. Borrelli, "Fabrication and analysis of a directional coupler written in glass by nanojoule femtosecond laser pulses," *Optics Letters* 26(1): 42-43 (2001).

[7] K. Minoshima, A. M. Kowalevicz, I. Hartl, E. P. Ippen, and J. G. Fujimoto, "Photonic device fabrication in glass by use of nonlinear materials processing with a femtosecond laser oscillator," *Optics Letters* 26(19): 1516-18 (2001).

[8] K. Minoshima, A. M. Kowalevicz, E. P. Ippen, and J. G. Fujimoto, "Fabrication of coupled mode photonic devices in glass by nonlinear femtosecond laser materials processing," *Optics Express* 10(15): (2002).

[9] C. Florea and K. A. Winick, "Fabrication and characterization of photonic devices directly written in glass using femtosecond laser pulses," *Journal of Lightwave Technology* 21(1): 246-53 (2003).

[10] R. Osellame, S. Taccheo, M. Marangoni, R. Ramponi, P. Laporta, D. Polli, S. De Silvestri, and G. Cerullo, "Femtosecond writing of active optical waveguides with astigmatically shaped beams," *Journal of the Optical Society of America B (Optical Physics)* 20(7): 1559-67 (2003).

[11] Y. Sikorski, A. A. Said, P. Bado, R. Maynard, C. Florea, and K. A. Winick, "Optical waveguide amplifier in Nd-doped glass written with near-IR femtosecond laser pulses," *Electronics Letters* 36(3): 226-27 (2000).

[12] S. Nolte, M. Will, J. Burghoff, and A. Tuennermann, "Femtosecond waveguide writing: a new avenue to three-dimensional integrated optics," *Applied Physics a-Materials Science & Processing* 77(1): 109-11 (2003).

[13] V. Sharma, A. M. Kowalevicz Jr, R. Huber, J. G. Fujimoto, and K. Minoshima, "Three dimensional waveguide splitters fabricated in glass using a femtosecond laser oscillator," paper presented at Conference on Lasers and Electro-Optics, CLEO, Baltimore, MD, May 22-27, 2005.

[14] Y. Nasu, M. Kohtoku, Y. Hibino, and Y. Inoue, "Three-dimensional waveguide interconnection in planar lightwave circuits by direct writing with femtosecond laser," *Japanese Journal of Applied Physics Part 2-Letters & Express Letters* 44(46-49): L1446-L48 (2005).

[15] W. Watanabe, T. Asano, K. Yamada, K. Itoh, and J. Nishii, "Wavelength division with three-dimensional couplers fabricated by filamentation of femtosecond laser pulses," *Optics Letters* 28(24): 2491-93 (2003).

[16] A. M. Kowalevicz, V. Sharma, E. P. Ippen, J. G. Fujimoto, and K. Minoshima, "Three-dimensional photonic devices fabricated in glass by use of a femtosecond laser oscillator," *Optics Letters* 30(9): 1060-2 (2005).

[17] K. Suzuki, V. Sharma, J. G. Fujimoto, and E. P. Ippen, "Characterization of symmetric [3x3] directional couplers fabricated by direct writing with a femtosecond laser oscillator," *Optics Express* 14(6): 2335-43 (2006).

[18] S. K. Sheem, "Optical Fiber Interferometers with [3by3] Directional-Couplers - Analysis," *Journal of Applied Physics* 52(6): 3865-72 (1981).

[19] K. Takada, H. Yamada, and M. Horiguchi, "Optical Low-Coherence Reflectometer Using [3x3] Fiber Coupler," *Ieee Photonics Technology Letters* 6(8): 1014-16 (1994).

[20] M. A. Choma, C. H. Yang, and J. A. Izatt, "Instantaneous quadrature low-coherence interferometry with 3 x 3 fiber-optic couplers," *Optics Letters* 28(22): 2162-64 (2003).

[21] R. Osellame, N. Chiodo, V. Maselli, A. Yin, M. Zavelani-Rossi, G. Cerullo, P. Laporta, L. Aiello, S. De Nicola, P. Ferraro, A. Finizio, and G. Pierattini, "Optical properties of waveguides written by a 26 MHz stretched cavity Ti:sapphire femtosecond oscillator," *Optics Express* 13(2): 612-20 (2005).

References in Refereed Journals Acknowledging FA9550-04-0011

1. P.B. Phua, H.A. Haus and E.P. Ippen, "Deterministic Broad-band PMD Emulator," IEEE Photon. Technol. Lett., 16 , pp.1486-1488, 2004.
2. R.P. Prasankumar, I. Hartl, J.T. Gopinath, E.P. Ippen, J.G. Fujimoto, P. Mak and M.F. Ruane, "Design and Characterization of Semiconductor-doped Silica Film Saturable Absorbers," J. Opt. Soc. Am. B., 21, pp. 851-857, 2004.
3. A. Sennaroglu, A.M. Kowalevicz, Jr., E.P. Ippen and J.G. Fujimoto, "Compact Femtosecond Lasers Based on Novel Multipass Cavities," IEEE J. Quant. Electron., 40, pp. 519-528, 2004.
4. H. Sotobayashi, J. T. Gopinath, E. M. Koontz, L. A. Kolodziejski and E. P.Ippen, "Wavelength Tunable Passively Mode-locked Bismuth Oxide-based Erbium-doped Fiber Laser," Opt. Commun., 237, pp.399-403, 2004
5. M.E. Grein, H.A. Haus, Y. Chen and E.P. Ippen, "Quantum-Limited Timing Jitter in Actively Modelocked Lasers," IEEE J. Quant. Electron. 40, pp. 1458-1471, 2004
6. J. T. Gopinath, M. Soljacic, E. P. Ippen, V. N. Fuflyigin, W.A. King and M. Shurgalin, "Third-order Nonlinearities in Ge-As-Se-based Glasses for Telecommunication Applications," J. Appl. Phys. 96, pp. 6931-6933, 2004
7. P.C. Wagenblast, T.H. Ko, J.G. Fujimoto, F.X. Kaertner, and U. Morgener, "Ultrahigh-resolution ophthalmic optical coherence tomography with diode-pumped broad-band Cr:LiCAF laser," Opt. Exp. 12, 3257-3263, 2004
8. P.R. Herz, Y. Chen, A.D. Aguirre, J.G., Fujimoto, H. Mashimo, J. Schmitt, A. Koski, J. Goodnow, and C. Petersen, "Ultrahigh resolution optical biopsy with endoscopic optical coherence tomography," Opt. Exp. 12, 3532-3542, 2004
9. G. Wollstein, J.S. Schuman, L.L. Price, A. Aydin, S.A. Beaton, P.C. Stark, J.G. Fujimoto, and H. Ishikawa, "Optical coherence tomography (OCT) macular and peripapillary retinal nerve fiber layer measurements and automated visual fields," Am. J. Ophthal. 138, 218-225, 2004
10. P. B. Phua, E. P. Ippen, "Fast Recursive Algorithm for Broadband APFs using Complex Cepstrums," Opt. Express, 12, p.4896-4904, 2004
11. J. T. Gopinath, H. M. Shen, H. Sotobayashi, E. P. Ippen, T. Hasegawa, T. Nagashima, N. Sugimoto, "Highly Nonlinear Bismuth-Oxide Fiber for Smooth Supercontinuum Generation at 1.5 μm," Opt. Express,12, p.5697-5702, 2004
12. L.E. Jiang, E.P. Ippen and H. Yokoyama, "Semiconductor Mode-locked Lasers as Pulse Sources for High Bit Rate Data Transmission," J. Opt. Fiber Commun. Rep., H-G. Weber and M. Nakazawa, eds., 1, pp. 1-31, 2004
13. F. X. Kärtner, E. P. Ippen and S. T. Cundiff, "Femtosecond laser development," in Femtosecond Optical Frequency Comb: Principle, Operation and Applications ed. J. Ye and S. T. Cundiff, Springer Verlag 2005.
14. S. Akiyama, F. J. Grawert, J. Liu, K. Wada, L. C. Kimerling and F. X. Kärtner, "Fabrication of highly reflecting epitaxy-ready Si/SiO2 Bragg reflectors," IEEE Photonics Technology Letters 17, 1456-1458 (2005).
15. F. J. Grawert, S. Akiyama, J. T. Gopinath, F. Ö. Ilday, H. Shen, J. Liu, K. Wada, L. C. Kimerling, E. P. Ippen and F. X. Kärtner, "220-fs erbium-ytterbium:glass laser mode locked by a broadband low-loss silicon_germanium saturable absorber," Opt. Lett. 30, 329-331, 2005.

16. T. M. Liu, F. X. Kärtner and J. G. Fujimoto, "Multiplying the repetition rate of passive mode-locked femtosecond lasers by an intracavity flat surface with low reflectivity," Opt. Lett. 30, 439-441, 2005

17. F. Gan and F. X. Kärtner, "High-Speed Silicon Electro-Optic Modulator Design," IEEE Photonics Technology Letters, 17, 1007-1010, 2005.

18. F. J. Grawert, F. Ö. Ilday, D. Kielpinski, J. T. Gopinath, L. A. Kolodziejski, G. S. Petrich, E.P. Ippen and F. X. Kärtner, "Automatic feedback control of an Er-doped fiber laser with an intracavity loss modulator," Opt. Lett. 30, 1066-1068, 2005.

19. F. Ö. Ilday, J. Chen, and F. X. Kärtner, "Generation of sub-100-fs pulses at up to 200 MHz repetition rate from a passively mode-locked Yb fiber laser," Optics Express 13, 2716-2718, 2005.

20. Ch. Jirauschek, L. Duane, O. D. Mücke, F. X. Kärtner, "Carrier-envelope phase sensitive inversion in two-level systems," J. of the Opt. Soc. of Am. B 22, 2065-2075, 2005.

21. O. D. Muecke, R. Ell, A. Winter, J. W. Kim, J. R. Birge, L. Matos, and F.X. Kärtner, "Self-Referenced 200 MHz Octave-Spanning Ti:Sapphire Laser with 50 Attosecond Carrier-Envelope Phase Jitter," Optics Express 13, 5163-5168, 2005

22. R. Ell, G. Angelow, W. Seitz, M. J. Lederer, H. Huber, D. Kopf, J. R. Birge, F. X. Kärtner, "Quasi-synchronous pumping of few-cycle Ti:sapphire lasers," Opt. Express, 13, pp.9292-8 (2005)

23. P.B. Phua and E.P. Ippen, "A Deterministic Broad-Band Polarization-Dependent Loss Compensator," J. Lightwave Technology, 23, pp. 771-780, 2005.

24. P. T. Rakich, H. Sotobayashi, J. T. Gopinath, S. G. Johnson, J. W. Sickler, C. W. Wong, J. D. Joannopoulos and E. P. Ippen, "Nano-scale Photonic Crystal Microcavity Characterization with an All-Fiber based 1.2 - 2.0 μm Supercontinuum," Opt. Express, 13, p. 821-825, 2005

25. A. M. Kowalevicz, V. Sharma, E. P. Ippen, J. G. Fujimoto, K. Minoshima, "Three-dimensional photonic devices fabricated in glass by use of a femtosecond laser oscillator," Opt. Lett., 30, pp.1060-2, 2005

26. J.T. Gopinath, H.M. Shen, H. Sotobayashi, E.P. Ippen, T. Hasegawa, T. Nagashima and N. Sugimoto, "Highly Nonlinear Bismuth-Oxide Fiber for Supercontinuum Generation and Femtosecond Pulse Compression," J. Lightwave Technology, 23, pp. 3591-3596 (2005)

27. A. Gordon and F. X. Kärtner, "Scaling of KeV HHG efficiency with drive wavelength," Optics Express, 13, 2941-2946, 2005

28. A. Gordon and F. X. Kärtner, "Quantitave modelling of single atom high harmonic generation," Physical Review Letters 95, 223901, 2005

29. T. Binhammer, E. Rittweger, R. Ell, F.X. Kärtner, and U. Morgner, "Novel prism-based pulse shaper for octave spanning spectra," IEEE J. Quant. Electron., 41, pp.1552-7, 2005

30. T.M. Liu, F.X. Kärtner, J.G. Fujimoto, and C.-K. Sun, "Multiplying the repetition rate of passive mode-locked femtosecond lasers by an intracavity flat surface with low reflectivity," Opt. Lett. 30, pp. 439-441, 2005.

31. R. Huber, M. Wojtkowski, K. Taira, J.G. Fujimoto, and K. Hsu, "Amplified, frequency swept lasers for frequency domain reflectometry and OCT imaging: design and scaling principles," Opt. Exp. 13, pp. 3513-3528, 2005.

32. J. Kim, J.R. Birge, V. Sharma, J.G. Fujimoto, F.X. Kärtner, V. Scheuer, and G. Angelow, "Ultrabroadband beam splitter with matched group-delay dispersion," Opt. Lett. 30, pp. 1569-1571, 2005.

33. A. Gordon, R. Santra and F. X. Kärtner, "Role of the Coulomb singularity in high harmonic generation", Phys. Rev. A **72**, 063411 (2005).

34. F. Ö. Ilday and F. X. Kärtner, "Cavity-enhanced optical parametric chirped-pulse amplification with nonlinearity management," Opt. Lett. 31, 637 (2006).

35. P.T. Rakich, M.S. Dahlem, S. Tandon, M. Ibanescu, M. Soljacic, G.S. Petrich, J.D. Joannopoulos, L.A. Kolodziejski and E.P. Ippen, "Achieving Centimetre-Scale Supercollimation in a Large-Area Two-Dimensional Photonic Crystal," Nature, doi: 10.1038, pp. 1-4, 2006

36. P.T. Rakich, M.A. Popovic, M.R. Watts, T. Barwicz, H.I. Smith and E.P. Ippen, "Ultrawide Tuning of Photonic Microcavities via Evanescent Field Perturbation," Opt. Lett., 31, pp. 1241-1243, 2006

Patent Submissions

1. Synchronization of lasers and RF sources using timing information transfer in the optical domain, (J. W. Kim , F. X. Kärtner and M. Perrott) MIT Case 18834.

2. Multi-layer thin-film broadband beam splitter with matched group delay dispersion, (J. W. Kim and F. X. Kärtner) MIT Case 10835.

3. Cavity-enhanced optical parametric chirped pulse amplification (F. X. Kärtner and F. Ö. Ilday) MIT Case 10963.